energies

MDPI

Article

Study of Generalized Interaction Wake Models Systems with ELM Variation for Off-Shore Wind Farms

Mingcan Li [1,†], Hanbin Xiao [1,†], Lin Pan [1,2,3,*] and Chengjun Xu [1,†]

1 School of Logistics Engineering, Wuhan University of Technology, Wuhan 430063, China; mclichina@126.com (M.L.); xhbchina@126.com (H.X.); xcjwhut@163.com (C.X.)
2 National Engineering Research Center for Water Transport Safety (WTS Center), Wuhan 430063, China
3 State Key Laboratory of Ocean Engineering, Shanghai Jiaotong University, Shanghai 200240, China
* Correspondence: lin.pan@whut.edu.cn
† These authors contributed equally to this work.

Received: 20 January 2019; Accepted: 28 February 2019; Published: 5 March 2019

Abstract: This paper reports a novel frandsen generalized wake model and its variation model-frandsen generalized normal distribution wake model for off-shore wind farms. Two different new wake models in off-shore wind farms have been studied comparatively. Their characteristics have been analyzed through mathematical modeling and derivation. Meanwhile, simulation experiments show that the proposed two new wake models have different properties. Furthermore, the distributions of wind speed and wind direction are modeled by the statistical methods and Extreme Learning Machine through the off-shore wind farms of Yangshan Deepwater Harbor in the Port of Shanghai, China. In addition, the data of wind energy are provided to verify and test the correctness and effectiveness of the proposed two models. Wind power has been demonstrated by wind rose and wind resources with real-time data. These techniques contribute to enhance planning, utilization and exploitation for wind power of off-shore wind farms.

Keywords: off-shore wind farms (OSWFs); wake model; wind turbine (WT); Extreme Learning Machine (ELM); wind power (WP); large-eddy simulation (LES)

1. Introduction

The global warming and the climate changes lead to a gradual shift from conventional to renewable energy sources which are more reliable clean resources. The main reason is the growing trend of global energy demands accompanied with the detrimental effects of overuse conventional fossil fuel sources namely [1–3].

Wind is one of the fastest growing energy sources, and it is also pollution-free, renewable and abundant. At present, some researchers have done a lot of research work on wind energy [4,5]. For example, based on short term wind speed forecasting of variable weight, Li et al. provided the research and application of a combined model [6]. Romanic et al. studied wind and tornado climatologies and wind resource modelling for a modern development situated in 'Tornado Alley' [7]. Ahmed Shata Ahmed investigated wind energy characteristics and wind park installation in Shark El-Ouinat, Egypt [8]. Using standard exergy and Extended Exergy Accounting (EEA) approaches, Aghbashlo et al. studied performance assessment of a wind power plant [9].

Wind energy has a low carbon footprint, which is a type of renewable energy. Some researchers and experts believe that local power generation sources like micro-grids on wind farm or micro power sources are better, in view of transmission efficiency and grid laying cost [10]. Some of the methods by

which sustainable energy can be harvested are solar, wind, vibration, tidal, etc. Ideally, a power source should be sustainable, reliable, economical and eco-friendly [11,12].

Among renewable energy sources, Wind Power (WP) is considered to be one of the most prospective renewable energy technologies, and its usage has been increased immensely over recent decades. Usually, Horizontal Axis Wind Turbines (HAWTs) as types of wind energy converters are a kind of medium to large scale rotating machinery and their technologies have been developed substantially during the last decades, resulting in significant performance improvement. Despite the considerable achievements in the aerodynamic improvement of the HAWTs, wind energy still has certain drawbacks that make the popularity of the wind turbine technology difficult.

Due to the location optimization caused by operation in the unsteady flow condition and dynamic loading exerted on the Wind Turbine (WT), one of its main problems is how to increase performance of the control system as decision-making, which makes the most effective use of the WT controller. The WT location optimization is an interesting topic, which provides a predominant approach to increase the total WP of the Wind Farm (WF) and decreases the wake effect of WTs [13–15]. In recent years, the size of WTs has been more extensive from a few kilowatts to several megawatts. Lots of experiences have shown that the larger the WTs, the lower the cost per kilowatt installed [16]. Furthermore, their total costs of production, installation and maintenance are less than the total of smaller WTs achieving the same WP [17]. In 2013, Chen et al. investigated tower height matching optimization for WT positioning in the wind farm [18]. One scheme for properly handling these aerodynamic interactions is to use and promote wake models in the optimization and distributed algorithms control. An alternative approach is to present an online control method where each WT adjusts its own sense model coefficients, which is in line with the communication of local Wind Farms (WFs) [19–21]. For example, V. Seshadri Sravan Kumar and D.Thukaram presented accurate modeling of doubly fed induction generator [22] based WFs in load flow analysis. Farajzadeh et al. proposed statistical modeling of the power grid from a wind farm standpoint [23]. Tian et al. developed and verified a new WT wake model with two dimensions in 2015 [24–27].

It is worth mentioning that Wind Energy (WE) has developed rapidly in China in recent years. For example, Figures 1 and 2 show off-shore wind farms (OSWFs) of Yangshan Deepwater Harbor in the Port of Shanghai, China, which is one of the largest wide range or scope WFs in China [28,29].

From the control point of view, the research of WFs has attracted a great deal of interest from researchers. Recently, Ebrahimi et al. proposed a new optimizing power control scheme based on a centralizing WF control system [30]. Song et al. presented the decision model of WF layout design with three dimensions [31]. Sadegh Ghani Varzaneh et al. have studied a novel simplified model for assessment of power alteration of Doubly-fed Induction Generator (DFIG) [32] based wind farm participating in frequency control system. Hossain has presented a nonlinear controller for transient stability enhancement of DFIG based new bridge type fault current limiter [33] for WFs. Yao et al. studied coordinated control of hybrid WFs [34] in a Permanent Magnet Synchronous Generator (PMSG) based and fixed-speed induction generator (FSIG) for WTs during an asymmetrical grid fault. Li et al. also proposed adaptive fault lenient control of WTs with safeguard transient performance considering active power control of WFs [35]. From met-mast and remote sensing techniques, Chaurasiya et al. proposed comparative analysis of Weibull parameters with wind data measured [36]. Hamid Atighechi et al. presented an effective load shedding remedial action strategy [37] for WF generation. Suganthi et al. proposed an Improved Differential Evolution algorithm [38] based on congestion management in the presence of wind turbine generators.

Figure 1. China's first off-shore wind farm in Yangshan Port.

Figure 2. Off-shore wind farm of Yangshan Deepwater Harbor in the Port of Shanghai, China.

Recently, there are some machine learning techniques used in such prediction of wind direction and wind speed for OSWFs. For example, Wan et al. proposed an Extreme Learning Machine (ELM) based method of probabilistic forecasting for wind power generation [39]. Vlastimir Nikolić et al. presented a novel wake model based upon ELM for sensor-less computation of wind speed based on WT parameters in WFs [40]. Lazarevska presented an alternative approach to forecasting the wind speed based on Extreme Learning Machine [41]. Wu et al. presented a real-time precise wind speed estimation approach and sensor-less control for variable pitch and variable speed Wind Turbine Power Generation System (WTPGS) [42].

Based on the above discussion, in general, the main contributions of this paper are as follows. Firstly, a Frandsen Generalized Wake Model (FGWM) and its variation model-Frandsen Generalized Normal Distribution Wake Model (FGNDWM) for WFs have been analyzed and presented with mathematical derivation forms. Then, comparisons of these two different wake models of OSWFs have been presented. Furthermore, comparative experiments of both Wake Models have been studied. Finally, focused on the OSWFs of Yangshan Deepwater Harbor in the Port of Shanghai, China, wind rose, wind Weibull probability density distribution and ELM prediction are elaborated and discussed through the OSWFs of Yangshan Harbor. Simulation figures are also provided to show the effectiveness of the proposed approach.

The structure of the paper is as follows: FGWM and FGNDWM are derived and studied in Sections 2 and 3. Meanwhile, in Sections 4 and 5, comparative analysis and experiments for the proposed two novel different wake models are studied. Furthermore, in Section 6, the wind rose, wind Weibull probability density distribution and ELM prediction are proposed for OSWFs of Yangshan Deepwater Harbor in the Port of Shanghai, China. Finally, in Section 7, the conclusions are summarized.

2. A Frandsen Generalized Wake Model (FGWM) for OSWFs

Frandsen Generalized Wake Model (FGWM) in the ideal state is shown in Figure 3, where the far wake area is described by the sideways trapezoidal region. The near field is denoted WT_{1ij} (radius is r_{1ij}) and can be seen as a turbulent wake. In the down-wind distance x_{ij}, the wind speed denoted P_{1ij} and P_{2ij} are assumed to be equal v_{0ij}, and the wind speed on S_{xij} is given by v_{xij}. The circular cross-section radius is r_{xij}, where i and j are row vector and column vector for Wind Turbine in large-scale Wind Farms, respectively.

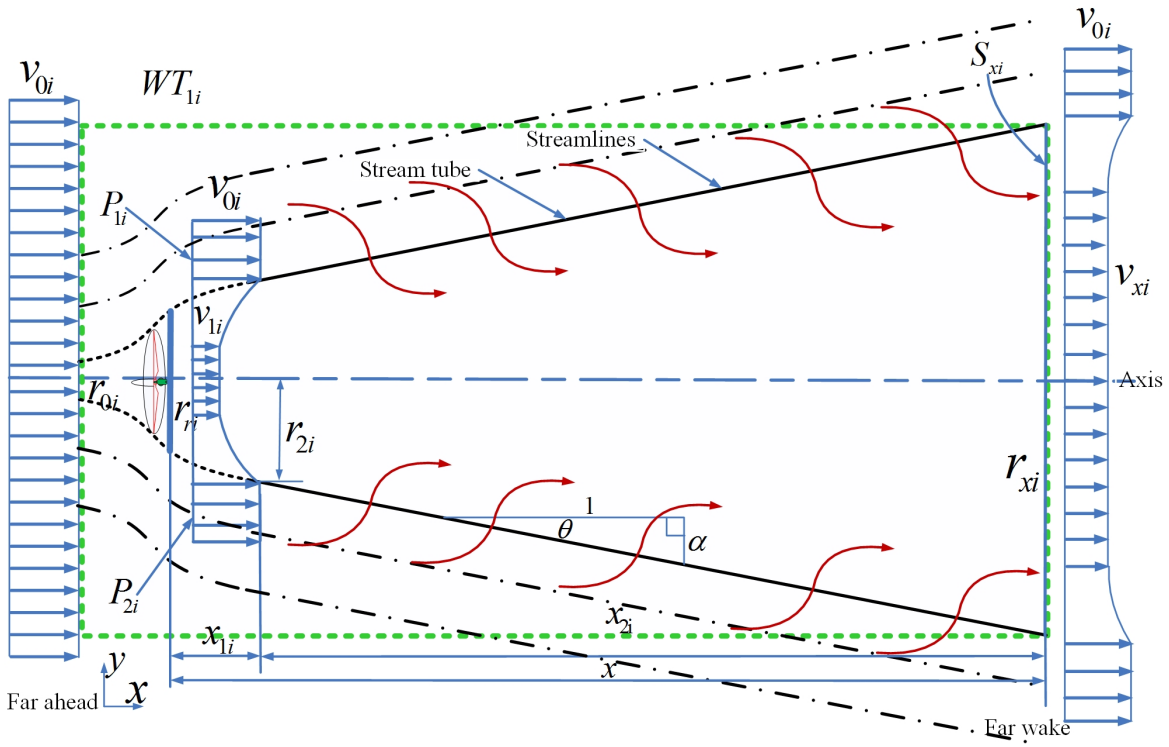

Figure 3. The portrait of Frandsen Generalized Wake Model (FGWM) with stream tube [43].

In an ideal state, the model assumes that the far wake region spreads with a linear approach, and the distribution of wind speed is homogeneous on every cross-section. In FGWM, the tube includes the near wake area, which is described in the green rectangular region in Figure 3. The fluid inlet mass flow rate in the tube is equal to $\sum_{i=1}^{n}\sum_{j=1}^{m}\rho\pi r_{xij}^2 v_{0ij}$ and it goes through the WT. The fluid outlet mass flow rate is equal to $\sum_{i=1}^{n}\sum_{j=1}^{m}\rho\pi r_{xij}^2 v_{xij}$. The FGWM assumes

$$\sum_{i=1}^{n}\sum_{j=1}^{m}\dot{M}_{ij} = \sum_{i=1}^{n}\sum_{j=1}^{m}\frac{\partial M_{ij}}{\partial t_{ij}} = \sum_{i=1}^{n}\sum_{j=1}^{m}\rho\pi r_{xij}^2 v_{xij}, \tag{1}$$

for $n = 1, 2, \cdots, N$; $m = 1, 2, \cdots, N$.

By conservation of momentum, we obtain

$$\begin{aligned}\sum_{i=1}^{n}\sum_{j=1}^{m}T_{ij} &= \sum_{i=1}^{n}\sum_{j=1}^{m}\left(\dot{M}_{ij}v_{0i} - \dot{M}_{ij}v_{xij}\right)\\ &= \sum_{i=1}^{n}\sum_{j=1}^{m}\left(\frac{\partial M_{ij}}{\partial t_{ij}}v_{0ij} - \frac{\partial M_{ij}}{\partial t_{ij}}v_{xij}\right),\end{aligned} \tag{2}$$

for $n = 1, 2, \cdots, N$; $m = 1, 2, \cdots, N$.

We assume that the radius of the row vector ith and column vector jth actuator disk is r_{rij}, then the area of ith $\times$ jth actuator disk is given as $A_{rij} = \pi r_{rij}^2$. According to the definition of thrust coefficient C_{Tij}, one can have

$$\begin{aligned}\sum_{i=1}^{n}\sum_{j=1}^{m} C_{Tij} &= \sum_{i=1}^{n}\sum_{j=1}^{m} \frac{T_{ThrustForceij}}{T_{DynamicForceij}} \\ &= \sum_{i=1}^{n}\sum_{j=1}^{m} \frac{T_{ij}}{T_{ijmax}} \\ &= \sum_{i=1}^{n}\sum_{j=1}^{m} \left[\frac{\frac{1}{2}\rho(v_{0ij}^2 - v_{xij}^2)A_{rij}}{\frac{1}{2}\rho v_{0ij}^2 A_{rij}}\right] \\ &= \sum_{i=1}^{n}\sum_{j=1}^{m} \left[\frac{2\rho v_{0ij}^2 A_{rij} a_{ij}(1-a_{ij})}{\frac{1}{2}\rho v_{0ij}^2 A_{rij}}\right],\end{aligned} \tag{3}$$

which is equivalent to

$$\sum_{i=1}^{n}\sum_{j=1}^{m} T_{ij} = \sum_{i=1}^{n}\sum_{j=1}^{m} C_{Tij} T_{ijmax}. \tag{4}$$

Substituting Equations (1), (3) and (4) into Equation (2), we obtain the following equation:

$$\sum_{i=1}^{n}\sum_{j=1}^{m} \left[v_{xij}^2 - v_{0i}v_{xij} + \frac{1}{2}C_{Tij}(\frac{r_{rij}}{r_{xij}})^2 v_{0ij}\right] = 0. \tag{5}$$

Solving Equation (5), one can have the following equation:

$$\begin{aligned}\sum_{i=1}^{n}\sum_{j=1}^{m} v_{xij} &= \sum_{i=1}^{n}\sum_{j=1}^{m} \frac{v_{0ij} \pm \sqrt{v_{0ij}^2 - 2C_{Tij}(\frac{r_{rij}}{r_{xij}})^2 v_{0ij}^2}}{2} \\ &= \sum_{i=1}^{n}\sum_{j=1}^{m} \left[\frac{1}{2} \pm \frac{1}{2}\sqrt{1 - \frac{2C_{Tij}}{(r_{xij}/r_{ri})^2}}\right] v_{0ij} \\ &= \sum_{i=1}^{n}\sum_{j=1}^{m} \left\{1 - \frac{1}{2}\left[1 \pm \sqrt{1 - \frac{2C_{Tij}}{(r_{xij}/r_{rij})^2}}\right]\right\} v_{0ij}.\end{aligned} \tag{6}$$

Using the physical solution of Equation (6), then we obtain

$$\sum_{i=1}^{n}\sum_{j=1}^{m} v_{xij} = \sum_{i=1}^{n}\sum_{j=1}^{m} \left\{1 - \frac{1}{2}\left[1 - \sqrt{1 - \frac{2C_{Tij}}{(r_{xij}/r_{rij})^2}}\right]\right\} v_{0ij}. \tag{7}$$

The above equation gives the main variables and results of the FGWM.

3. A Frandsen Generalized Normal Distribution Wake Model (FGNDWM) for OSWFs

The Frandsen Generalized Normal Distribution Wake Model (FGNDWM) called Frandsen Generalized Gaussian Distribution Wake Model (FGGDWM) for OSWFs is illustrated in Figure 4 where the two dotted lines A_{ij} and C_{ij} are selected to be the boundaries of the FGNDWM tube. The far wake region is confined to the dotted line tube region while the farthest boundary is extended to infinity. The wind speed on P_{1ij} and P_{2ij} are recognized as v_{0ij} and the wind speed on S_{xij} is v_{xij}. Here, i and j are row vector and column vector for Wind Turbine in large-scale offshore Wind Farms, respectively.

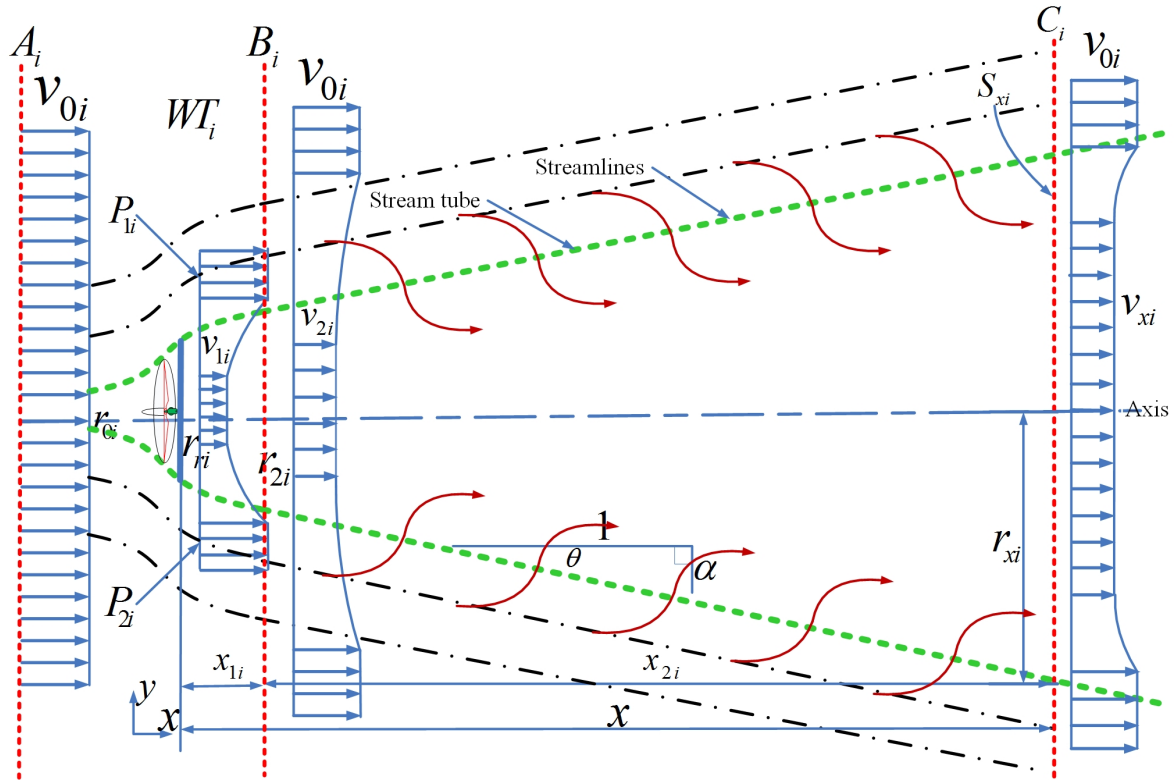

Figure 4. The portrait of Frandsen Generalized Normal Distribution Wake Model (FGNDWM) with stream.

The conservation of mass does not hold comparing to the FGWM. The following equation is considered as the outlet mass flow rate

$$\sum_{i=1}^{n}\sum_{j=1}^{m}\dot{M}_{ij}=\frac{\partial M_{ij}}{\partial t}=\sum_{i=1}^{n}\sum_{j=1}^{m}\int_{0}^{+\infty}2\pi r_{xij}\rho v_{x_{ij},r_{xij}}dr_{xij},$$
$$n=1,2,\cdots,N;\ m=1,2,\cdots,N. \tag{8}$$

The FGNDWM satisfies the following equation:

$$\sum_{i=1}^{n}\sum_{j=1}^{m}v_{x_{ij},r_{xij}}=\sum_{i=1}^{n}\sum_{j=1}^{m}\left[1-\Psi(x_{ij})\exp\left(-\frac{r_{ij}^{2}}{2\sigma_{ij}^{2}}\right)\right]v_{0ij}, \tag{9}$$

where σ_{ij} is the standard deviation, which is also called the characteristic width of FGNDWM and $\Psi(x_{ij})$ is a coefficient related to x_{ij}.

According to the momentum conservation law, one can obtain the following result

$$\sum_{i=1}^{n}\sum_{j=1}^{m}\int_{0}^{+\infty}2\pi r_{xij}\rho v_{x_{ij},r_{xij}}\left(v_{0i}-v_{xij,r_{xij}}\right)dr_{xij}=\sum_{i=1}^{n}\sum_{j=1}^{m}T_{ij}, \tag{10}$$

which is equivalent to

$$\sum_{i=1}^{n}\sum_{j=1}^{m}\lim_{b\to+\infty}\int_{0}^{b}2\pi r_{xij}\rho v_{x_{ij},r_{xij}}\left(v_{0ij}-v_{xij,r_{xij}}\right)dr_{xij}$$
$$=\sum_{i=1}^{n}\sum_{j=1}^{m}T_{ij}. \tag{11}$$

From the definition of the thrust coefficient, one can have the following equation:

$$\begin{aligned}\sum_{i=1}^{n}\sum_{j=1}^{m} T_{ij} = C_{Tij}T_{ij_{max}} &= \frac{1}{2}\sum_{i=1}^{n}\sum_{j=1}^{m}\rho A_{rij}v_{0i}^2 C_{Tij} \\ &= \frac{1}{2}\sum_{i=1}^{n}\sum_{j=1}^{m}\rho\pi r_{rij}^2 v_{0ij}^2 C_{Tij}.\end{aligned} \tag{12}$$

Substituting Equations (9) and (12) into Equation (11), we obtain

$$\begin{aligned}&\sum_{i=1}^{n}\sum_{j=1}^{m}\lim_{b\to+\infty}\int_0^b 2\pi r_{xij}\rho v_{x_{ij},r_{xij}}(v_{0i}-v_{xij,r_{xij}})dr_{xij} \\ &= \sum_{i=1}^{n}\sum_{j=1}^{m} C_{Tij}T_{ij_{max}}.\end{aligned} \tag{13}$$

From this equation, we obtain:

$$\begin{aligned}&\sum_{i=1}^{n}\sum_{j=1}^{m}\lim_{b\to+\infty}\int_0^b 2\pi r_{xij}\rho v_{0ij}^2\left[1-\Psi(x_{ij})\exp\left(-\frac{r_{ij}^2}{2\sigma_{ij}^2}\right)\right]dr_{ij} \\ &-\sum_{i=1}^{n}\sum_{j=1}^{m}\lim_{b\to+\infty}\int_0^b 2\pi r_{xij}\rho v_{0ij}^2\left[1-\Psi(x_{ij})\exp\left(-\frac{r_{ij}^2}{2\sigma_{ij}^2}\right)\right]^2 dr_{ij} \\ &= \sum_{i=1}^{n}\sum_{j=1}^{m}\frac{1}{2}\rho\pi r_{rij}^2 v_{0ij}^2 C_{Tij}, \quad n=1,2,\cdots,N;\ m=1,2,\cdots,N,\end{aligned} \tag{14}$$

which is also equivalent to

$$\begin{aligned}&\sum_{i=1}^{n}\sum_{j=1}^{m}\lim_{b\to+\infty}\int_0^b 2r_{xij}\left[1-\Psi(x_{ij})\exp\left(-\frac{r_{ij}^2}{2\sigma_{ij}^2}\right)\right]dr_{ij} \\ &-\sum_{i=1}^{n}\sum_{j=1}^{m}\lim_{b\to+\infty}\int_0^b 2r_{xij}\left[1-\Psi(x_{ij})\exp\left(-\frac{r_{ij}^2}{2\sigma_{ij}^2}\right)\right]^2 dr_{ij} \\ &= \sum_{i=1}^{n}\sum_{j=1}^{m}\frac{1}{2}r_{rij}^2 C_{Tij}, \quad n=1,2,\cdots,N;\ m=1,2,\cdots,N.\end{aligned} \tag{15}$$

Computing this equation, then we have

$$\begin{aligned}
&\sum_{i=1}^{n}\sum_{j=1}^{m}\lim_{b\to+\infty}\frac{r_{xij}}{2}\Big|_0^b \\
&-\sum_{i=1}^{n}\sum_{j=1}^{m}\lim_{b\to+\infty}\int_0^b \Psi(x_{ij})\exp\left(-\frac{r_{ij}^2}{2\sigma_{ij}^2}\right)r_{ij}dr_{ij} \\
&-\sum_{i=1}^{n}\sum_{j=1}^{m}\lim_{b\to+\infty}\frac{r_{xij}}{2}\Big|_0^b \\
&+2\sum_{i=1}^{n}\sum_{j=1}^{m}\lim_{b\to+\infty}\int_0^b \Psi(x_{ij})\exp\left(-\frac{r_{ij}^2}{2\sigma_{ij}^2}\right)r_{ij}dr_{ij} \\
&-\sum_{i=1}^{n}\sum_{j=1}^{m}\lim_{b\to+\infty}\int_0^b \Psi^2(x_{ij})\exp\left(-\frac{2r_{ij}^2}{2\sigma_{ij}^2}\right)r_{ij}dr_{ij} \\
&=\sum_{i=1}^{n}\sum_{j=1}^{m}\frac{1}{4}r_{rij}^2C_{Tij},\quad n=1,2,\cdots,N;\ m=1,2,\cdots,N
\end{aligned} \tag{16}$$

or also

$$\begin{aligned}
&\sum_{i=1}^{n}\sum_{j=1}^{m}\lim_{b\to+\infty}\int_0^b \Psi(x_{ij})\exp\left(-\frac{r_{ij}^2}{2\sigma_{i}^2}\right)r_{ij}dr_{ij} \\
&\quad-\sum_{i=1}^{n}\sum_{j=1}^{m}\lim_{b\to+\infty}\int_0^b \Psi^2(x_{ij})\exp\left(-\frac{r_{ij}^2}{\sigma_{i}^2}\right)r_{ij}dr_{ij} \\
&=\sum_{i=1}^{n}\sum_{j=1}^{m}\frac{1}{4}r_{rij}^2C_{Tij},\quad n=1,2,\cdots,N;\ m=1,2,\cdots,N,
\end{aligned} \tag{17}$$

which can be also written as

$$\begin{aligned}
&-\sum_{i=1}^{n}\sum_{j=1}^{m}\lim_{b\to+\infty}\Psi(x_{ij})\sigma_{ij}^2\exp\left(-\frac{r_{xij}^2}{2\sigma_{ij}^2}\right)\Big|_0^b \\
&\quad+\sum_{i=1}^{n}\sum_{j=1}^{m}\lim_{b\to+\infty}\Psi^2(x_{ij})\frac{\sigma_{ij}^2}{2}\exp\left(-\frac{r_{ij}^2}{\sigma_{ij}^2}\right)\Big|_0^b \\
&=\sum_{i=1}^{n}\sum_{j=1}^{m}\frac{1}{4}r_{rij}^2C_{Tij},\quad n=1,2,\cdots,N;\ m=1,2,\cdots,N.
\end{aligned} \tag{18}$$

Then, we obtain

$$\begin{aligned}
&\sum_{i=1}^{n}\sum_{j=1}^{m}\left[\Psi(x_{ij})\sigma_{ij}^2-\Psi^2(x_{ij})\frac{\sigma_{ij}^2}{2}\right]=\sum_{i=1}^{n}\sum_{j=1}^{m}\left(\frac{1}{4}C_{Tij}r_{rij}^2\right), \\
&\quad n=1,2,\cdots,N;\ m=1,2,\cdots,N,
\end{aligned} \tag{19}$$

which is

$$\begin{aligned}
&\sum_{i=1}^{n}\sum_{j=1}^{m}\left[\Psi^2(x_{ij})-2\Psi(x_{ij})+\frac{1}{2}C_{Tij}\left(\frac{r_{rij}}{\sigma_{ij}}\right)^2\right]=0, \\
&\quad n=1,2,\cdots,N;\ m=1,2,\cdots,N,
\end{aligned} \tag{20}$$

or equivalently

$$\sum_{i=1}^{n}\sum_{j=1}^{m}\left[\Psi^2(x_{ij})-2\Psi(x_{ij})+\frac{C_{Tij}}{2\left(\frac{\sigma_{ij}}{r_{rij}}\right)^2}\right]=0, \quad n=1,2,\cdots,N;\ m=1,2,\cdots,N. \tag{21}$$

By solving Equation (21), we obtain

$$\begin{aligned}\sum_{i=1}^{n}\sum_{j=1}^{m}\Psi(x_{ij}) &= \sum_{i=1}^{n}\sum_{j=1}^{m}\frac{2\pm\sqrt{4-2\frac{C_{Tij}}{(\sigma_{ij}/r_{rij})^2}}}{2}\\ &= \sum_{i=1}^{n}\sum_{j=1}^{m}\left[1\pm\sqrt{1-\frac{C_{Tij}}{2(\sigma_{ij}/r_{rij})^2}}\right]\\ &= \sum_{i=1}^{n}\sum_{j=1}^{m}\left[1\pm\sqrt{1-\frac{C_{Tij}}{2}\left(\frac{r_{rij}}{\sigma_{ij}}\right)^2}\right],\\ n=1,2,\cdots,N;\ m=1,2,\cdots,N.\end{aligned} \tag{22}$$

From Equation (22), the physical solution is

$$\sum_{i=1}^{n}\sum_{j=1}^{m}\Psi(x_{ij})=\sum_{i=1}^{n}\sum_{j=1}^{m}\left[1-\sqrt{1-\frac{C_{Tij}}{2}\left(\frac{r_{rij}}{\sigma_{ij}}\right)^2}\right], \quad n=1,2,\cdots,N;\ m=1,2,\cdots,N. \tag{23}$$

By substituting this solution into Equation (9), we obtain

$$\begin{aligned}&\sum_{i=1}^{n}\sum_{j=1}^{m}v_{x_{ij},r_{xij}}\\ &=\sum_{i=1}^{n}\sum_{j=1}^{m}\{1-\\ &\left[1-\sqrt{1-\frac{C_{Tij}}{2}\left(\frac{r_{rij}}{\sigma_{ij}}\right)^2}\right]\exp\left(-\frac{r_{ij}^2}{2\sigma_{ij}^2}\right)\Bigg\}v_{0ij},\\ &n=1,2,\cdots,N;\ m=1,2,\cdots,N.\end{aligned} \tag{24}$$

Here, σ_{ij} is recognized as a linear function of x_{ij} in FGNDWM. In FGWM and FGNDWM, owing to every plane is perpendicular to the axis, the rates of mass flow are equal to each other in both FGWM and FGNDWM. According to the law of mass conservation, we can calculate and get:

$$\begin{aligned}&\sum_{i=1}^{n}\sum_{j=1}^{m}\int_0^{+\infty}2\pi r_{ij}\rho_{ij}v_{x_{ij},r_{xij}}dr_{ij}\\ &=\sum_{i=1}^{n}\sum_{j=1}^{m}\int_0^{r_{xij}}2\pi r_{ij}\rho_{ij}v_{xij}dr_{ij}+\sum_{i=1}^{n}\sum_{j=1}^{m}\int_{r_{xij}}^{+\infty}2\pi r_{ij}\rho_i v_{0ij}dr_{ij},\\ &n=1,2,\cdots,N;\ m=1,2,\cdots,N,\end{aligned} \tag{25}$$

which is

$$\begin{aligned}
&\sum_{i=1}^{n}\sum_{j=1}^{m}\lim_{b\to+\infty}\int_0^b 2\pi r_{ij}\rho_{ij}v_{x_{ij},r_{xij}}dr_{ij}\\
&=\sum_{i=1}^{n}\sum_{j=1}^{m}\int_0^{r_{xij}} 2\pi r_{ij}\rho_{ij}v_{xij}dr_{ij}\\
&+\sum_{i=1}^{n}\sum_{j=1}^{m}\lim_{b\to+\infty}\int_{r_{xij}}^b 2\pi r_{ij}\rho_{ij}v_{0ij}dr_{ij},\\
&n=1,2,\cdots,N;\ m=1,2,\cdots,N.
\end{aligned} \tag{26}$$

Substituting Equations (7) and (24) into Equation (26), we obtain

$$\begin{aligned}
&\sum_{i=1}^{n}\sum_{j=1}^{m}\lim_{b\to+\infty}\int_0^b 2\pi r_{ij}\rho_{ij}\{1\\
&-\left[1-\sqrt{1-\frac{C_{Tij}}{2}\left(\frac{r_{rij}}{\sigma_{ij}}\right)^2}\right]\exp\left(-\frac{r_{ij}^2}{2\sigma_{ij}^2}\right)\Bigg\}v_{0ij}dr_{ij}\\
&=\sum_{i=1}^{n}\sum_{j=1}^{m}\int_0^{r_{xij}} 2\pi r_{ij}\rho_{ij}\{1\\
&-\frac{1}{2}\left[1-\sqrt{1-\frac{2C_{Tij}}{(r_{xij}/r_{rij})^2}}\right]\Bigg\}v_{0ij}dr_{ij}\\
&+\sum_{i=1}^{n}\sum_{j=1}^{m}\lim_{b\to+\infty}\int_{r_{xij}}^b 2\pi r_{ij}\rho_{ij}v_{0ij}dr_{ij},\\
&n=1,2,\cdots,N;\ m=1,2,\cdots,N,
\end{aligned} \tag{27}$$

or equivalently

$$\begin{aligned}
&\sum_{i=1}^{n}\sum_{j=1}^{m}\lim_{b\to+\infty}\int_0^b r_{ij}\{1\\
&-\left[1-\sqrt{1-\frac{C_{Tij}}{2}\left(\frac{r_{rij}}{\sigma_{ij}}\right)^2}\right]\exp\left(-\frac{r_{ij}^2}{2\sigma_{ij}^2}\right)\Bigg\}dr_{ij}\\
&=\sum_{i=1}^{n}\sum_{j=1}^{m}\int_0^{r_{xij}} r_{ij}\left\{1-\frac{1}{2}\left[1-\sqrt{1-\frac{2C_{Tij}}{(r_{xij}/r_{rij})^2}}\right]\right\}dr_{ij}\\
&+\sum_{i=1}^{n}\sum_{j=1}^{m}\lim_{b\to+\infty}\int_{r_{xij}}^b r_{ij}dr_{ij},\\
&n=1,2,\cdots,N;\ m=1,2,\cdots,N,
\end{aligned} \tag{28}$$

which can be also written as

$$\begin{aligned}
&\sum_{i=1}^{n}\sum_{j=1}^{m}\lim_{b\to+\infty}\int_0^b r_{ij}dr_{ij}-\sum_{i=1}^{n}\sum_{j=1}^{m}[1-\\
&\sqrt{1-\frac{C_{Tij}}{2}\left(\frac{r_{rij}}{\sigma_i}\right)^2}\Bigg]\lim_{b\to+\infty}\int_0^b r_{ij}\exp\left(-\frac{r_{ij}^2}{2\sigma_{ij}^2}\right)dr_{ij}\\
&=\sum_{i=1}^{n}\sum_{j=1}^{m}\int_0^{r_{xij}} r_{ij}\left[\frac{1}{2}+\frac{1}{2}\sqrt{1-\frac{2C_{Tij}}{(r_{xij}/r_{rij})^2}}\right]dr_{ij}\\
&+\sum_{i=1}^{n}\sum_{j=1}^{m}\lim_{b\to+\infty}\int_{r_{xij}}^b r_{ij}dr_{ij}\\
&n=1,2,\cdots,N;\ m=1,2,\cdots,N,
\end{aligned}\tag{29}$$

or equivalently

$$\begin{aligned}
&\sum_{i=1}^{n}\sum_{j=1}^{m}\lim_{b\to+\infty}\frac{r_{ij}^2}{2}\Big|_0^b-\sum_{i=1}^{n}[1-\\
&\sqrt{1-\frac{C_{Tij}}{2}\left(\frac{r_{rij}}{\sigma_i}\right)^2}\Bigg]\lim_{b\to+\infty}\int_0^b r_{ij}\exp\left(-\frac{r_{ij}^2}{2\sigma_{ij}^2}\right)dr_{ij}\\
&=\sum_{i=1}^{n}\sum_{j=1}^{m}\frac{1}{2}\frac{r_i^2}{2}\Big|_0^{r_{xij}}+\sum_{i=1}^{n}\sum_{j=1}^{m}\frac{1}{2}\sqrt{1-\frac{2C_{Tij}}{(r_{xij}/r_{rij})^2}}\frac{r_{ij}^2}{2}\Big|_0^{r_{xij}}\\
&+\sum_{i=1}^{n}\sum_{j=1}^{m}\lim_{b\to+\infty}\frac{r_{ij}^2}{2}\Big|_{r_{rij}}^b\\
&n=1,2,\cdots,N;\ m=1,2,\cdots,N.
\end{aligned}\tag{30}$$

From Equation (30), we have

$$\begin{aligned}
&-\sum_{i=1}^{n}\sum_{j=1}^{m}[1-\\
&\sqrt{1-\frac{C_{Tij}}{2}\left(\frac{r_{rij}}{\sigma_{ij}}\right)^2}\Bigg]\lim_{b\to+\infty}\int_0^b r_{ij}\exp\left(-\frac{r_{ij}^2}{2\sigma_{ij}^2}\right)dr_{ij}\\
&=\sum_{i=1}^{n}\sum_{j=1}^{m}\frac{1}{2}\frac{r_{xij}^2}{2}+\sum_{i=1}^{n}\sum_{j=1}^{m}\frac{1}{2}\sqrt{1-\frac{2C_{Tij}}{(r_{xij}/r_{rij})^2}}\frac{r_{xij}^2}{2}-\sum_{i=1}^{n}\sum_{j=1}^{m}\frac{r_{xij}^2}{2}\\
&n=1,2,\cdots,N;\ m=1,2,\cdots,N,
\end{aligned}\tag{31}$$

which can be expressed by the following simple equation:

$$\begin{aligned}
&-\sum_{i=1}^{n}\sum_{j=1}^{m}\left[1-\sqrt{1-\frac{C_{Tij}}{2}\left(\frac{r_{rij}}{\sigma_{ij}}\right)^2}\right]\sigma_i^2\\
&=-\sum_{i=1}^{n}\sum_{j=1}^{m}\frac{r_{xij}^2}{4}+\sum_{i=1}^{n}\sum_{j=1}^{m}\frac{r_{xij}^2}{4}\sqrt{1-\frac{2C_{Tij}}{(r_{xij}/r_{rij})^2}}\\
&n=1,2,\cdots,N;\ m=1,2,\cdots,N
\end{aligned}\tag{32}$$

or also

$$\begin{aligned}&\sum_{i=1}^{n}\sum_{j=1}^{m}\left[1-\sqrt{1-\frac{C_{Tij}}{2}\left(\frac{r_{rij}}{\sigma_{ij}}\right)^2}\right]\sigma_{ij}^2\\&=\sum_{i=1}^{n}\sum_{j=1}^{m}\frac{r_{xij}^2}{4}-\sum_{i=1}^{n}\sum_{j=1}^{m}\frac{r_{xij}^2}{4}\sqrt{1-\frac{2C_{Tij}}{(r_{xij}/r_{rij})^2}}\\&n=1,2,\cdots,N;\ m=1,2,\cdots,N.\end{aligned}\tag{33}$$

Now, we can deduce the following results from Equation (33):

$$\begin{aligned}&\sum_{i=1}^{n}\sum_{j=1}^{m}\left[\sigma_{ij}^2-\sigma_{ij}\sqrt{\sigma_{ij}^2-\frac{C_{Tij}r_{rij}^2}{2}}\right]\\&=\sum_{i=1}^{n}\sum_{j=1}^{m}\frac{r_{xij}^2}{4}-\sum_{i=1}^{n}\sum_{j=1}^{m}\frac{r_{xij}^2}{4}\sqrt{1-\frac{2C_{Tij}}{(r_{xij}/r_{rij})^2}}\\&n=1,2,\cdots,N;\ m=1,2,\cdots,N,\end{aligned}\tag{34}$$

which leads to

$$\begin{aligned}&\sum_{i=1}^{n}\sum_{j=1}^{m}\left[\sigma_{ij}^2-\frac{r_{xij}^2}{4}\left(1-\sqrt{1-\frac{2C_{Tij}}{(r_{xij}/r_{rij})^2}}\right)\right]\\&=\sum_{i=1}^{n}\sum_{j=1}^{m}\sigma_{ij}\sqrt{\sigma_{ij}^2-\frac{C_{Tij}r_{rij}^2}{2}}\\&n=1,2,\cdots,N;\ m=1,2,\cdots,N.\end{aligned}\tag{35}$$

Now, by squaring the two sides of Equation (35), we obtain:

$$\begin{aligned}&\sum_{i=1}^{n}\sum_{j=1}^{m}\left[\sigma_{ij}^4-\frac{r_{xij}^2}{2}\sigma_{ij}^2\left(1-\sqrt{1-\frac{2C_{Tij}}{(r_{xij}/r_{rij})^2}}\right)\right.\\&\left.+\frac{r_{xij}^4}{16}\left(1-\sqrt{1-\frac{2C_{Tij}}{(r_{xij}/r_{rij})^2}}\right)^2\right]\\&=\sum_{i=1}^{n}\sum_{j=1}^{m}\sigma_{ij}^2\left(\sigma_{ij}^2-\frac{C_{Tij}r_{rij}^2}{2}\right)\\&n=1,2,\cdots,N;\ m=1,2,\cdots,N.\end{aligned}\tag{36}$$

By arranging the different terms, we obtain:

$$\begin{aligned}&\sum_{i=1}^{n}\sum_{j=1}^{m}\left[-\frac{r_{xij}^2}{2}\left(1-\sqrt{1-\frac{2C_{Tij}}{(r_{xij}/r_{rij})^2}}\right)\sigma_{ij}^2+\frac{C_{Tij}r_{rij}^2}{2}\sigma_{ij}^2\right]\\&=\sum_{i=1}^{n}\sum_{j=1}^{m}\left[-\frac{r_{xij}^4}{16}\left(1-\sqrt{1-\frac{2C_{Tij}}{(r_{xij}/r_{rij})^2}}\right)^2\right]\\&n=1,2,\cdots,N;\ m=1,2,\cdots,N,\end{aligned}\tag{37}$$

which gives the following equality:

$$\sum_{i=1}^{n}\sum_{j=1}^{m}\sigma_{ij}^{2}=\sum_{i=1}^{n}\sum_{j=1}^{m}\left[\frac{-\frac{r_{xij}^{4}}{16}\left(1-\sqrt{1-\frac{2C_{Tij}}{(r_{xij}/r_{rij})^{2}}}\right)^{2}}{-\frac{r_{xij}^{2}}{2}\left(1-\sqrt{1-\frac{2C_{Tij}}{(r_{xij}/r_{rij})^{2}}}\right)+\frac{C_{Tij}r_{rij}^{2}}{2}}\right] \tag{38}$$
$$n=1,2,\cdots,N;\ m=1,2,\cdots,N,$$

which can be rewritten as:

$$\begin{aligned}&\sum_{i=1}^{n}\sum_{j=1}^{m}\sigma_{ij}^{2}\\&=\sum_{i=1}^{n}\sum_{j=1}^{m}\left[\frac{-\frac{r_{xij}^{2}}{4}\times\frac{r_{xij}^{2}}{4}\left(1-2\sqrt{1-\frac{2C_{Tij}}{(r_{xij}/r_{rij})^{2}}}+1-\frac{2C_{Tij}}{(r_{xij}/r_{rij})^{2}}\right)}{-\frac{r_{xij}^{2}}{2}+\frac{r_{xij}^{2}}{2}\sqrt{1-\frac{2C_{Tij}}{(r_{xij}/r_{rij})^{2}}}+\frac{C_{Tij}r_{rij}^{2}}{2}}\right]\\&n=1,2,\cdots,N;\ m=1,2,\cdots,N,\end{aligned} \tag{39}$$

which is equivalent to:

$$\begin{aligned}&\sum_{i=1}^{n}\sum_{j=1}^{m}\sigma_{ij}^{2}\\&=\sum_{i=1}^{n}\sum_{j=1}^{m}\left[\frac{\frac{r_{xij}^{2}}{4}\left(-\frac{r_{xij}^{2}}{2}+\frac{r_{xij}^{2}}{2}\sqrt{1-\frac{2C_{Tij}}{(r_{xij}/r_{rij})^{2}}}+\frac{C_{Tij}r_{rij}^{2}}{2}\right)}{-\frac{r_{xij}^{2}}{2}+\frac{r_{xij}^{2}}{2}\sqrt{1-\frac{2C_{Tij}}{(r_{xij}/r_{rij})^{2}}}+\frac{C_{Tij}r_{rij}^{2}}{2}}\right]\\&n=1,2,\cdots,N;\ m=1,2,\cdots,N.\end{aligned} \tag{40}$$

Then, we deduce

$$\sum_{i=1}^{n}\sum_{j=1}^{m}\sigma_{ij}^{2}=\sum_{i=1}^{n}\sum_{j=1}^{m}\frac{r_{xij}^{2}}{4},\quad n=1,2,\cdots,N;\ m=1,2,\cdots,N, \tag{41}$$

which gives, for the real σ_i, the following value

$$\begin{aligned}\sum_{i=1}^{n}\sum_{j=1}^{m}\sigma_{ij}&=\sum_{i=1}^{n}\sum_{j=1}^{m}\frac{r_{xij}}{2}\\&=\sum_{i=1}^{n}\sum_{j=1}^{m}\frac{r_{0ij}+\alpha_{ij}x_{ij}}{2}\\&=\sum_{i=1}^{n}\sum_{j=1}^{m}\frac{r_{0ij}}{2}+\frac{\alpha_{ij}}{2}x_{ij},\\&\quad n=1,2,\cdots,N;\ m=1,2,\cdots,N,\end{aligned} \tag{42}$$

where $r_{xij}=r_{0ij}+\alpha_{ij}x_{ij}$, α_{ij} and r_{0ij} can be given and estimated empirically from

$$\sum_{i=1}^{n}\sum_{j=1}^{m}\alpha_{ij}=\sum_{i=1}^{n}\sum_{j=1}^{m}\frac{0.5}{\ln(z_{hij}/z_{0ij})},\quad n=1,2,\cdots,N;\ m=1,2,\cdots,N \tag{43}$$

and

$$\sum_{i=1}^{n}\sum_{j=1}^{m} r_{0ij} = \sum_{i=1}^{n}\sum_{j=1}^{m} \frac{4}{5} r_{2ij}, \quad n = 1, 2, \cdots, N;\ m = 1, 2, \cdots, N \tag{44}$$

in [44], respectively. Finally, Equations (9), (23), (24) and (42) constitute the FGNDWM.

4. Comparisons and Analysis of Two Different Wake Models for OSWFs

In this section, we will give the definition of Wind Speed Deficit (WSD) and further discuss the relationship between FGWM and FGNDWM. Usually, comparing WSD is a very important approach in different Wake Models. The WSD of OSWFs is expressed as by the following equation:

$$\frac{\Delta v_{ij}}{v_{0ij}} = \frac{v_{0ij} - v_{xij}}{v_{0ij}}, \quad i = 1, 2, \cdots, N; j = 1, 2, \cdots, N. \tag{45}$$

Firstly, the WSD of FGWM is derived by Equations (7) and (45):

$$\begin{aligned} \Delta v_{FGWM_{ij}} &= \frac{v_{0ij} - v_{x_{ij}}}{v_{0ij}} \\ &= \frac{v_{0ij} - \left\{1 - \frac{1}{2}\left[1 - \sqrt{1 - \frac{2C_{Tij}}{(r_{xij}/r_{rij})^2}}\right]\right\} v_{0ij}}{v_{0ij}} \\ &= \frac{1}{2}\left[1 - \sqrt{1 - \frac{2C_{Tij}}{(r_{xij}/r_{rij})^2}}\right], \\ & i = 1, 2, \cdots, N; j = 1, 2, \cdots, N. \end{aligned} \tag{46}$$

Meanwhile, we obtain the WSD of FGNDWM. With the condition: $r_{ij} = 0$, the WSD of FGNDWM on the axis is interpreted based on Equations (24) and (45):

$$\begin{aligned} \Delta v_{FGNDWM_{ij}} &= \frac{v_{0ij} - v_{x_{ij}, r_{ij}}}{v_{0ij}} \\ &= \frac{v_{0ij} - \left\{1 - \left[1 - \sqrt{1 - \frac{C_{Tij}}{2}\left(\frac{r_{rij}}{\sigma_{ij}}\right)^2}\right] \exp\left(-\frac{r_{ij}^2}{2\sigma_{ij}^2}\right)\right\} v_{0ij}}{v_{0ij}} \\ &= 1 - \sqrt{1 - \frac{C_{Tij}}{2}\left(\frac{r_{rij}}{\sigma_{ij}}\right)^2} \\ &= 1 - \sqrt{1 - \frac{C_{Tij}}{2\left(\frac{\sigma_{ij}}{r_{rij}}\right)^2}}, \quad i = 1, 2, \cdots, N; j = 1, 2, \cdots, N. \end{aligned} \tag{47}$$

Substituting $\sigma_{ij} = \frac{r_{xij}}{2}$ into Equation (47), we obtain

$$\begin{aligned}\Delta v_{FGNDWM_{ij}} &= \frac{v_{0ij} - v_{x_{ij},r_{ij}}}{v_{0ij}} \\ &= 1 - \sqrt{1 - \frac{C_{Tij}}{2}\left(\frac{r_{rij}}{\frac{r_{xij}}{2}}\right)^2} \\ &= 1 - \sqrt{1 - \frac{2C_{Tij}}{(r_{xij}/r_{rij})^2}}, \\ & i = 1, 2, \cdots, N; j = 1, 2, \cdots, N.\end{aligned} \tag{48}$$

The ratio of the WSD from FGWM to FGNDWM is calculated by Equations (46) and (48):

$$\begin{aligned}\frac{\Delta v_{FGWM_{ij}}}{\Delta v_{FGNDWM_{ij}}} &= \frac{\frac{1}{2}\left[1 - \sqrt{1 - \frac{2C_{Tij}}{(r_{xij}/r_{rij})^2}}\right]}{1 - \sqrt{1 - \frac{2C_{Tij}}{(r_{xij}/r_{rij})^2}}} \\ &= \frac{1}{2}, \quad i = 1, 2, \cdots, N; j = 1, 2, \cdots, N.\end{aligned} \tag{49}$$

We can find out the WSD of FGWM is half as small as that of FGNDWM on the axis.

5. Experimental Comparisons and Analysis of Two Different Wake Models for OSWFs

In this section, we collect and use data of five cases to confirm the different characteristics between FGWM and FGNDWM. Usually, using miniature WT with the Large-Eddy Simulation (LES) data was known as the standard case in the literature.

The main data and parameters of the five cases (OSWFs in Yangshan port, Shanghai) are shown in the following Table 1, in which z_{hij} is the height of the Hub, and z_{0ij} is the rate of surface sea or roughness. These roughness lengths shown for $Cases(b-e)$ in Table 1 are representative of different sea surface types, including very rough terrain, for instance, islands with different sizes ($z_{0ij} = 0.1$ m), sea surface with reefs, rocks and shoal rocks ($z_{0ij} = 0.01$ m), sea surface with medium waves and large waves ($z_{0ij} = 0.001$ m), and sea surface with small waves ($z_{0ij} = 0.00001$ m). d_{rij} is the diameter of the rotor, α_{ij} is the axial induction factor, r_{0ij} is the downstream rotor radius, C_{Tij} is the thrust coefficient, and v_{0ij} is cut-in wind speed. Here, i and j are row vector and column vector for Wind Turbine in large-scale offshore Wind Farms, respectively.

LES are applied in many fields of flow simulations. The initial conditions have a very significant influence on the LES results. $x_{ij}/d_{rij} = 3$ and $\Delta v_{ij}/v_{0ijmax} = 0.5$ were chosen as the initial conditions used for LES simulation conducted in this study.

Table 1. Different experiments and Large-Eddy Simulation (LES) case to validate the Generalized model of OSWFs in Yangshan port, Shanghai.

Cases	d_{rij} (m)	z_{hij} (m)	v_{0ij} (m/s)	C_{Tij}	z_{0ij} (m)	α_{ij}	r_{0ij} (m)
$Case_a$	0.15	0.125	2.2	0.4194	0.00003	0.119	0.066
$Case_b$	66	65	6	0.3916	0.1	0.11	38.08
$Case_c$	66	98	6	0.2944	0.01	0.08	40.48
$Case_d$	82	75	6	0.2256	0.001	0.06	43.52
$Case_e$	70	65	6	0.2256	0.00001	0.062	41.12

Note: $Case_a$ represents the Large-Eddy Simulation (LES) data; $Case_b$ represents OSWF-b in Yangshan port, Shanghai; $Case_c$ represents OSWF-c in Yangshan port, Shanghai; $Case_d$ represents OSWF-d in Yangshan port, Shanghai; $Case_e$ represents OSWF-e in Yangshan port, Shanghai.

Using some given data in Table 1, we conduct the simulation experiments with FGWM and FGNDWM. By analyzing Figures 5–9, from simulations and experiments, we can find the WSD of FGWM are half times smaller then that of FGNDWM on the axis. These simulations validate the results obtained in the last sections.

If the length of the near wake region x_{1i} is taken into consideration and the parameters are selected according to Table 1, the result is shown in Figure 5. The FGNDWM appeared superior to FGWM. The problem was that FGWM did not take x_{1i} into consideration, whereas the FGNDWM took it into consideration. In addition, the characteristic width of the FGNDWM was obtained by fitting the LES data in the experiment of this study.

It can be seen from Figure 8 that the accuracy of the FGNDWM and the FGWM is better than that in Figures 7 and 9. The maximum Wind Speed Deficit (WSD) of this FGNDWM can be proved to be twice as large as that of the FGWM; if α_{ij} and r_{0ij} are estimated by (43) and (44), respectively, the result is shown in Figure 9. As previously stated, (43) is not applicable to case *a* and case *e*. As a result, the accuracy of the FGNDWM and FGWM in Figure 6 is worse than that in Figures 5 and 7–9.

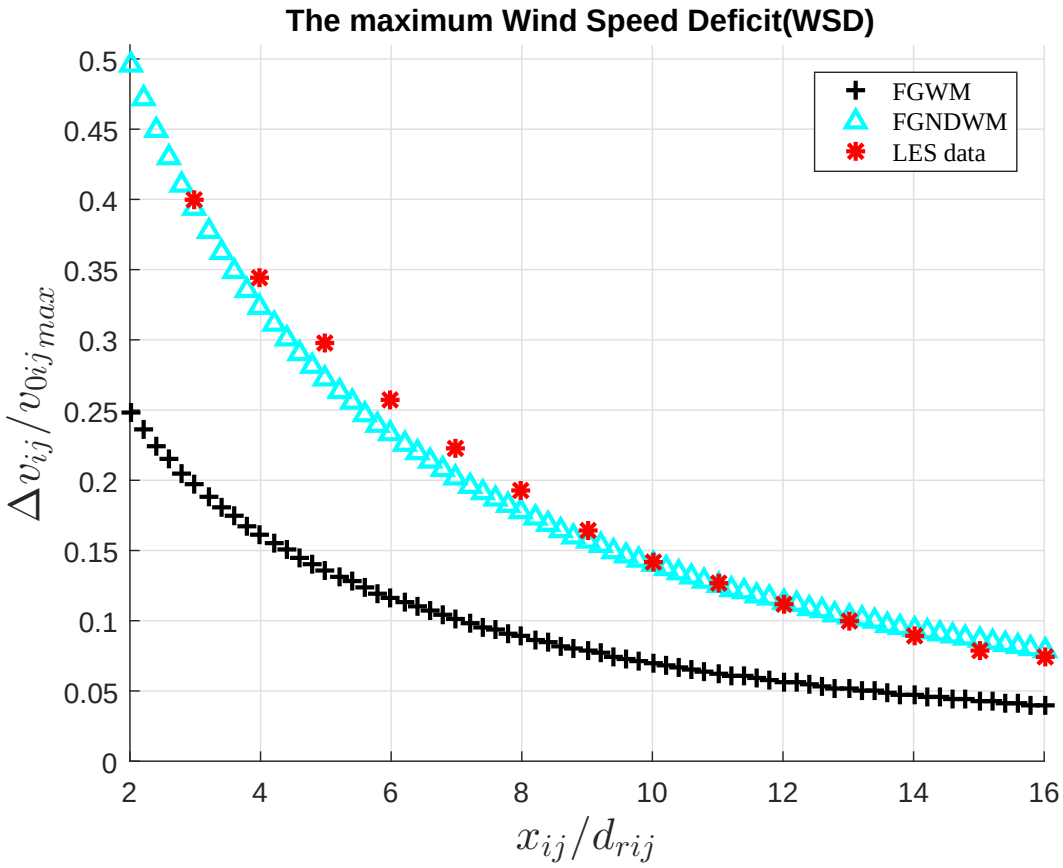

Figure 5. The portrait of the maximum Wind Speed Deficit (WSD) in $Case_a$ (fitted by LES data, $i = 1, 2, \cdots, N$; $j = 1, 2, \cdots, N$).

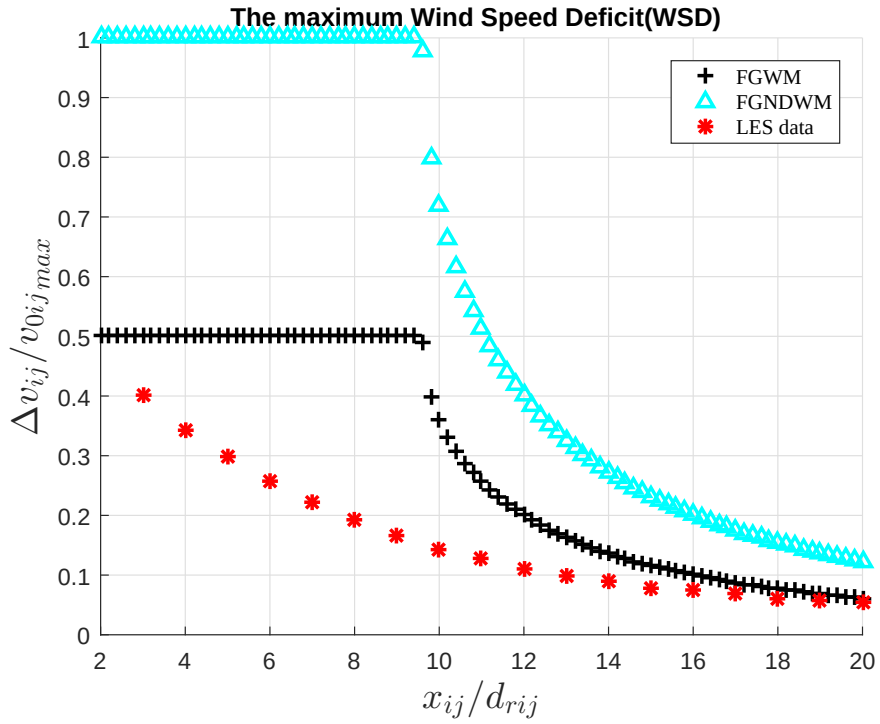

Figure 6. The portrait of the maximum Wind Speed Deficit (WSD) in $Case_b$ (fitted by LES data, $i = 1, 2, \cdots, N$; $j = 1, 2, \cdots, N$).

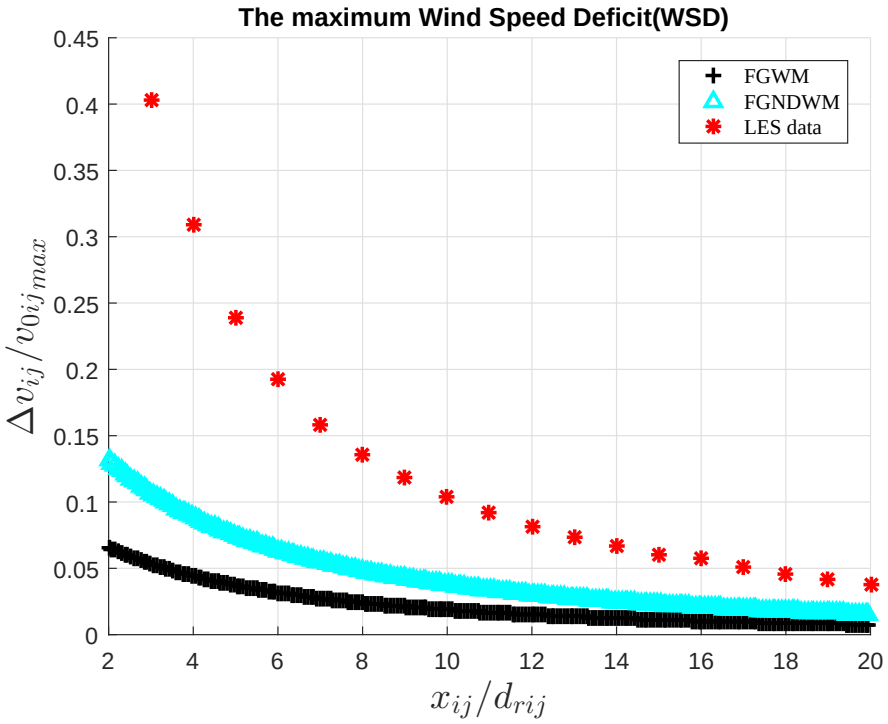

Figure 7. The portrait of the maximum Wind Speed Deficit (WSD) in $Case_c$ (fitted by LES data, $i = 1, 2, \cdots, N$; $j = 1, 2, \cdots, N$).

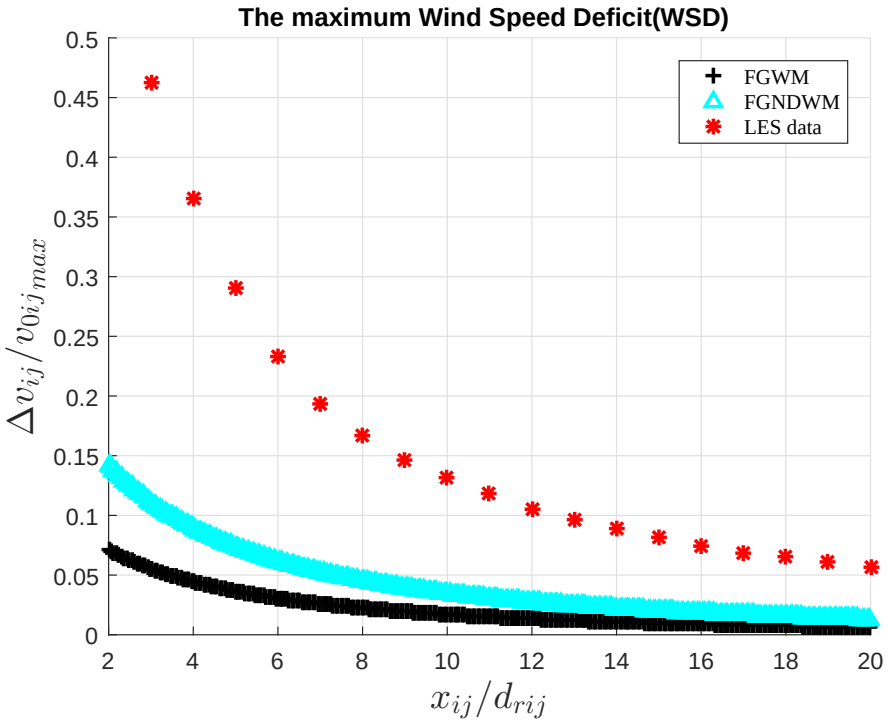

Figure 8. The portrait of the maximum Wind Speed Deficit (WSD) in $Case_d$ (fitted by LES data, $i = 1, 2, \cdots, N$; $j = 1, 2, \cdots, N$).

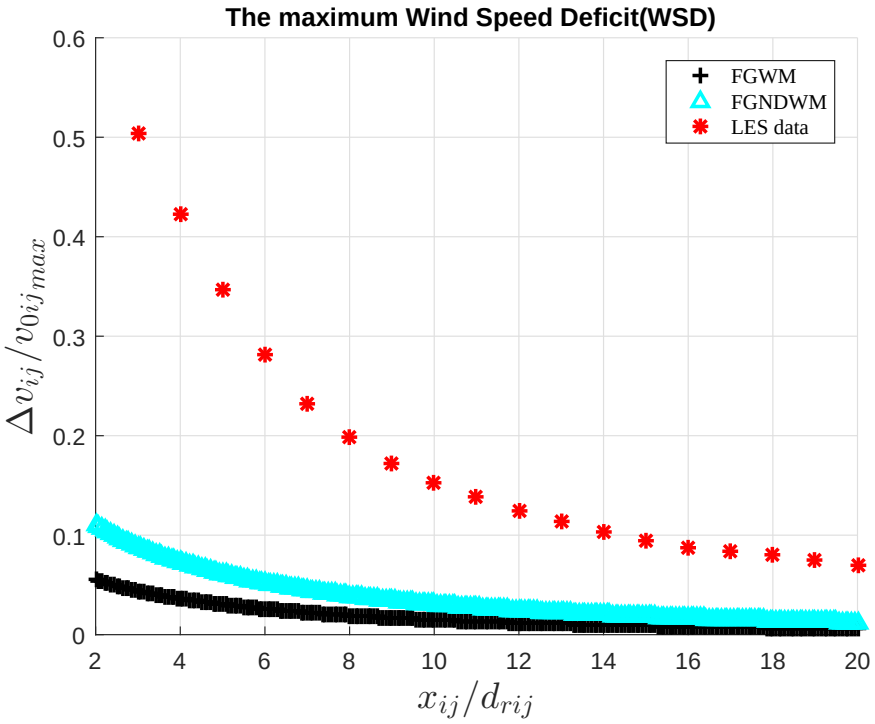

Figure 9. The portrait of the maximum Wind Speed Deficit (WSD) in $Case_e$ (fitted by LES data, $i = 1, 2, \cdots, N$; $j = 1, 2, \cdots, N$).

6. Analysis and Enlightenment of Wind Rose, Wind Weibull Probability Density Distribution and ELM Prediction

Based on the actual situation in OSWFs in Yangshan port, Shanghai, this section summarizes and describes the analysis of wind rose, wind Weibull probability density distribution and ELM prediction. We obtain the real-time and actual data from this website [45]. The WE cases are analyzed and studied based on mathematical models, and WRs are abstracted through the variable wind directions and wind speeds in OSWFs in Yangshan port, Shanghai. These data of WE resources are collected and shown in the following figures.

From 22 August 2017 to 22 August 2018, the portraits of wind direction and wind speed (m/s) in OSWFs of Yangshan port, Shanghai are shown with the wind rose in Figure 10. From the southwest direction, most of the wind mean speeds in a whole year are greater than 6 m/s, whereas, from the northwest direction, a small part of wind mean speeds are close to 6 m/s in a whole year.

From 22 August 2016 to 22 August 2017 with a whole year in OSWFs of Yangshan port, Shanghai, we keep obtaining the real-time and actual data from this website [45]. The wind speeds are collected and their Mean Wind Speed (MWS) is 3.4934 m/s. The details of them are shown in Figure 11.

From 22 August 2016 to 22 August 2017 with a whole year in OSWFs of Yangshan port, Shanghai, the rose portraits of Wind Direction (WD) and Average Wind Direction (AWD) are shown in Figure 12. Among them, the north direction is 0 degrees (North = 0 °C) . The probabilities of most of the parts of WDs from the southwest direction are greater than 5% and are close to 6%. Meanwhile, a small part of WD from the northeast direction is greater than 5% and close to 6%.

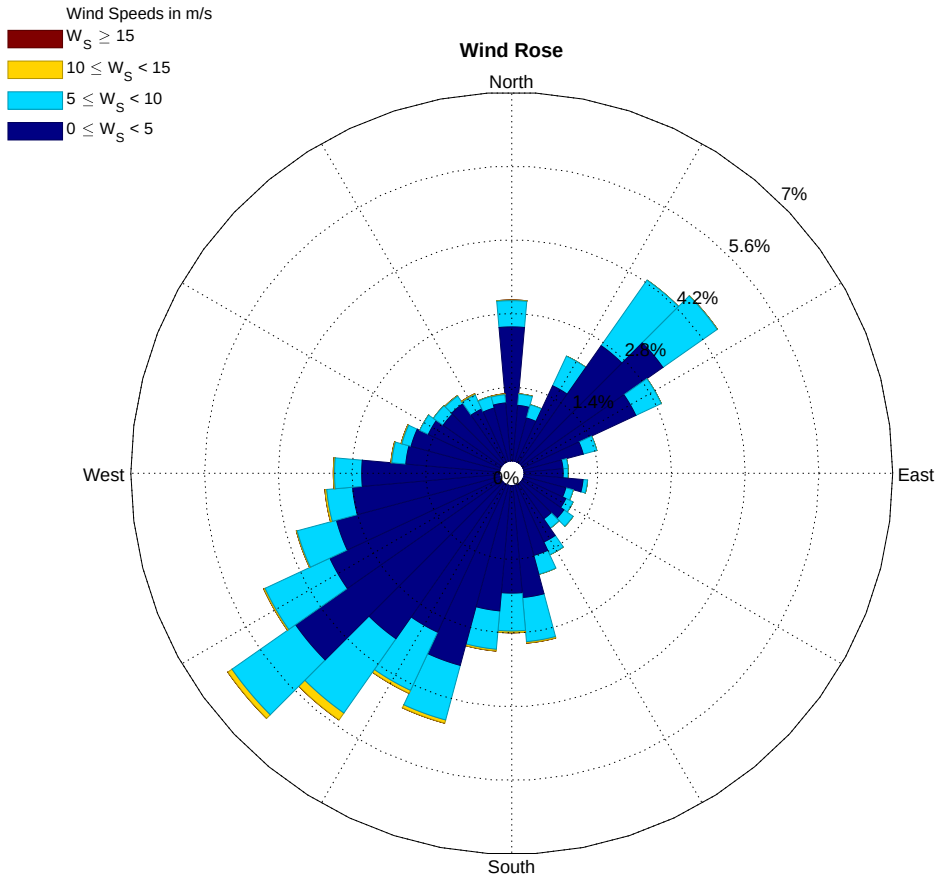

Figure 10. Rose portrait of WD (North = 0) and speed (m/s) in off-shore wind farms (OSWFs) in Yangshan port, Shanghai from 22 August 2017 to 22 August 2018.

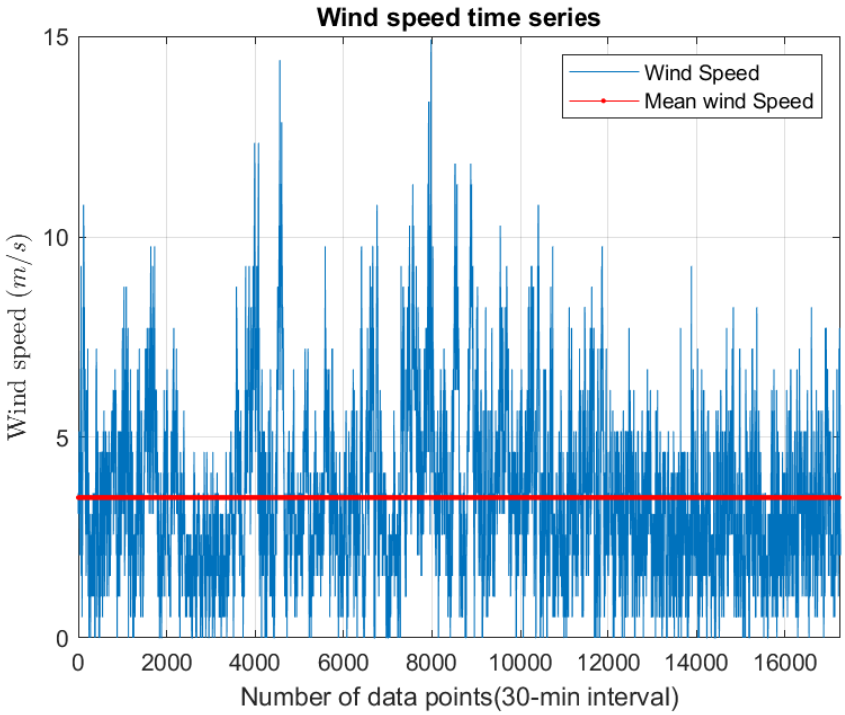

Figure 11. The portraits of wind speed time series and mean speed ($\bar{v} = 3.4934$ m/s) in OSWFs in Yangshan port, Shanghai from 22 August 2017 to 22 August 2018.

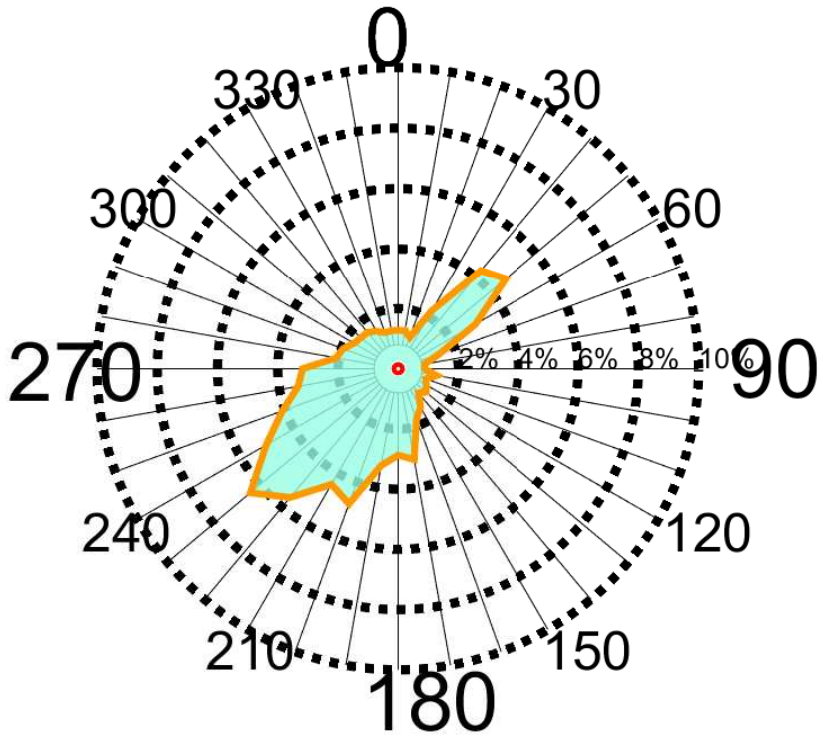

Figure 12. Rose portrait of WD (North direction = 0°) in OSWFs in Yangshan port, Shanghai from 22 August 2017 to 22 August 2018.

In Figure 13, the wind rose shows the portraits of wind mean speed (m/s) in OSWFs of Yangshan port, Shanghai from 22 August 2017 to 22 August 2018 with a whole year. The majority of the wind mean speeds from the southwest are greater than 5 m/s, whereas, a small amount of wind mean

speed from the northwest is approximate to 5 m/s. Therefore, WTs should adjust the direction to the southwest in OSWFs of Yangshan port, Shanghai throughout the summer, for even more periods.

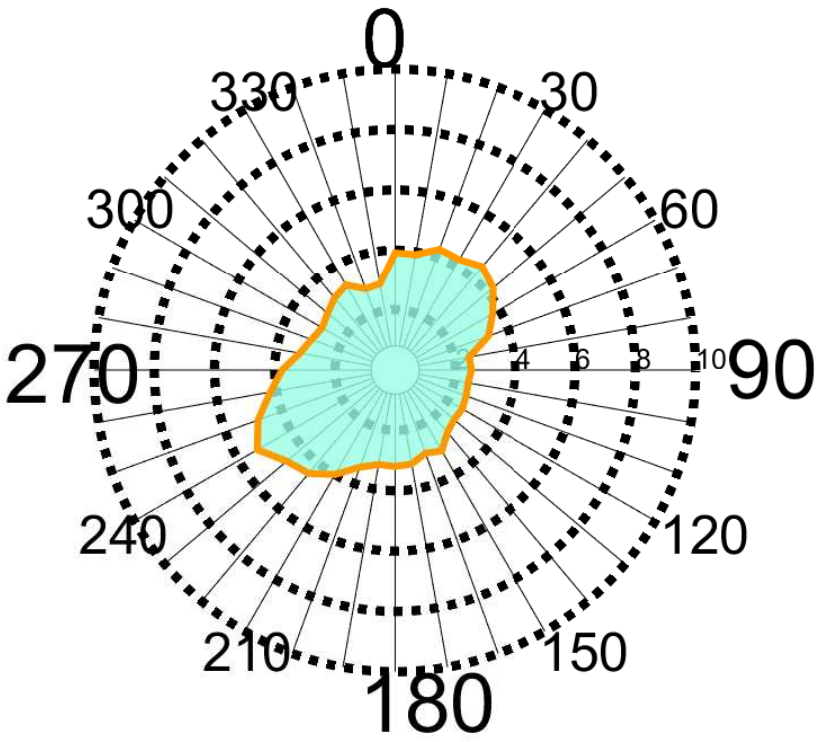

Figure 13. Rose portrait of Wind Mean Speed (m/s) in OSWFs of Yangshan port, Shanghai from 22 August 2017 to 22 August 2018.

Figures 14–16 show all the wind situations, including the time series of air relative humidity, wind direction and wind temperature in OSWFs in Yangshan port, Shanghai from 22 August 2017 to 22 August 2018, respectively. In this period, the mean air relative humidity is 82.0978%, the mean wind direction is 169.4492°(North direction = 0°), and the mean wind temperature is 10.0367 °C.

ELM is a learning algorithm, initially introduced to train a Single Layer Feedforward Neural network [46]. In ELM theory, the input weights are randomly generated according to any continuous distribution function, while the output weights are analytically computed by the minimum norm solution of a linear system.

Here, as shown in Figure 17, the proposed ELM can be seen as three hidden layer neural networks, trained using the ELM algorithm. ELM is applied to wind direction and wind speed prediction in OSWFs in Yangshan port, Shanghai from 22 August 2017 to 22 August 2018. The wind direction and wind speed of OSWFs are relevant to local air relative humidity and local wind temperature. Some simulation results show the corresponding rationality. Figures 18 and 19 show the portraits of comparison of wind direction and wind speed forecasting results with ELM in OSWFs in Yangshan port, Shanghai from 22 August 2017 to 22 August 2018, respectively. Here, the number of forecast data pieces is 2248. Figures 20 and 21 show the portraits of comparison of wind direction and wind speed forecasting results with ELM in OSWFs in Yangshan port, Shanghai from 22 August 2017 to 22 August 2018, respectively. At the same time, the number of forecast data pieces is 500.

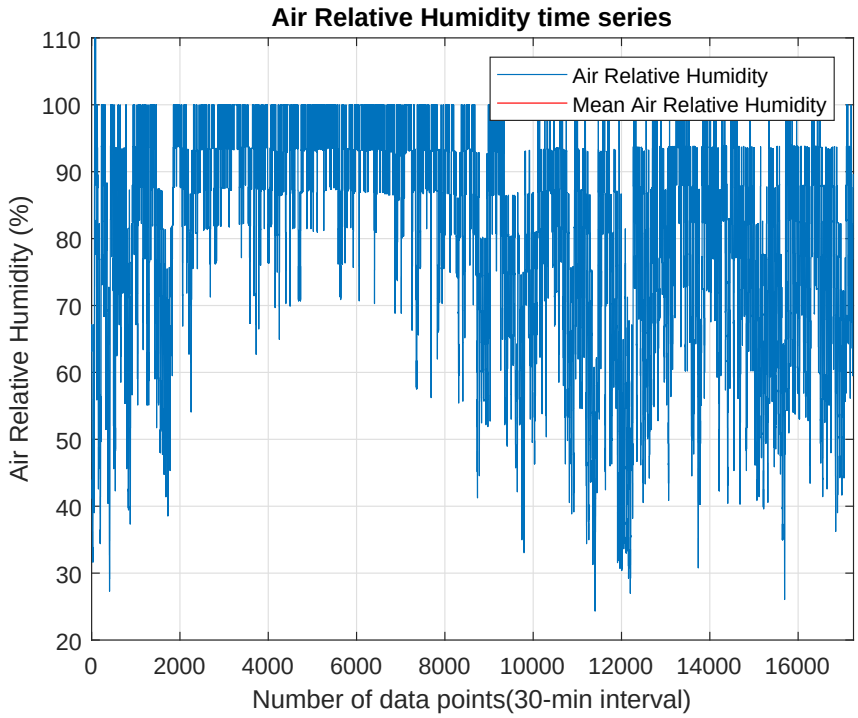

Figure 14. The portraits of air relative humidity in OSWFs in Yangshan port, Shanghai from 22 August 2017 to 22 August 2018.

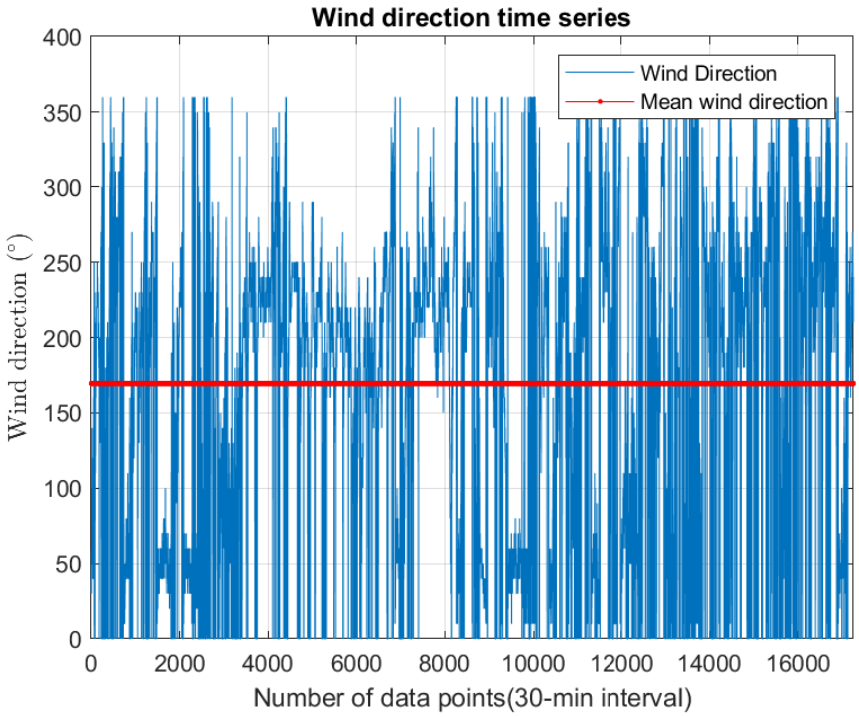

Figure 15. The portraits of wind direction (north direction = 0°) in OSWFs in Yangshan port, Shanghai from 22 August 2017 to 22 August 2018.

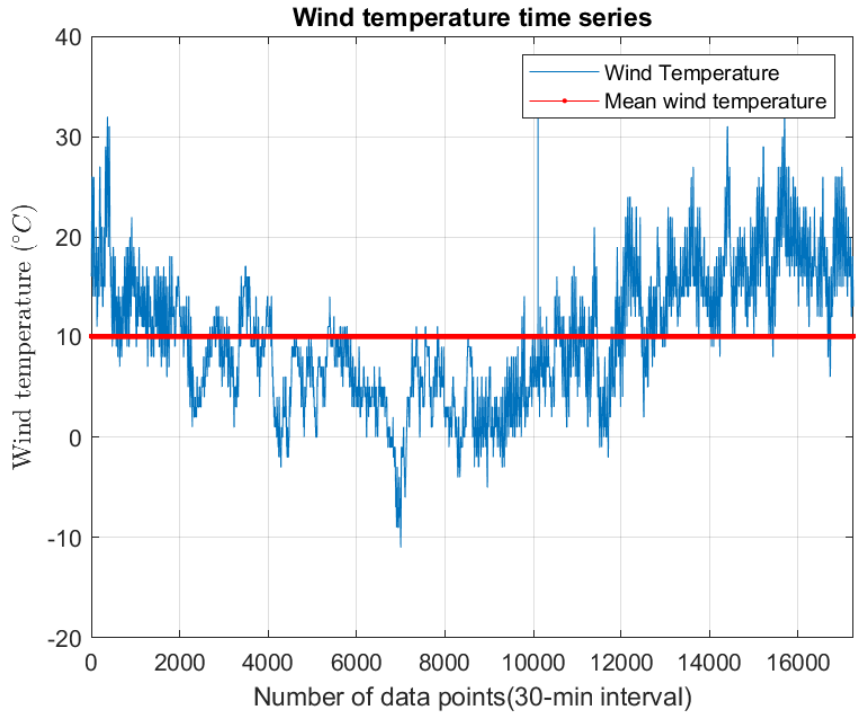

Figure 16. The portraits of wind temperature in OSWFs in Yangshan port, Shanghai from 22 August 2017 to 22 August 2018.

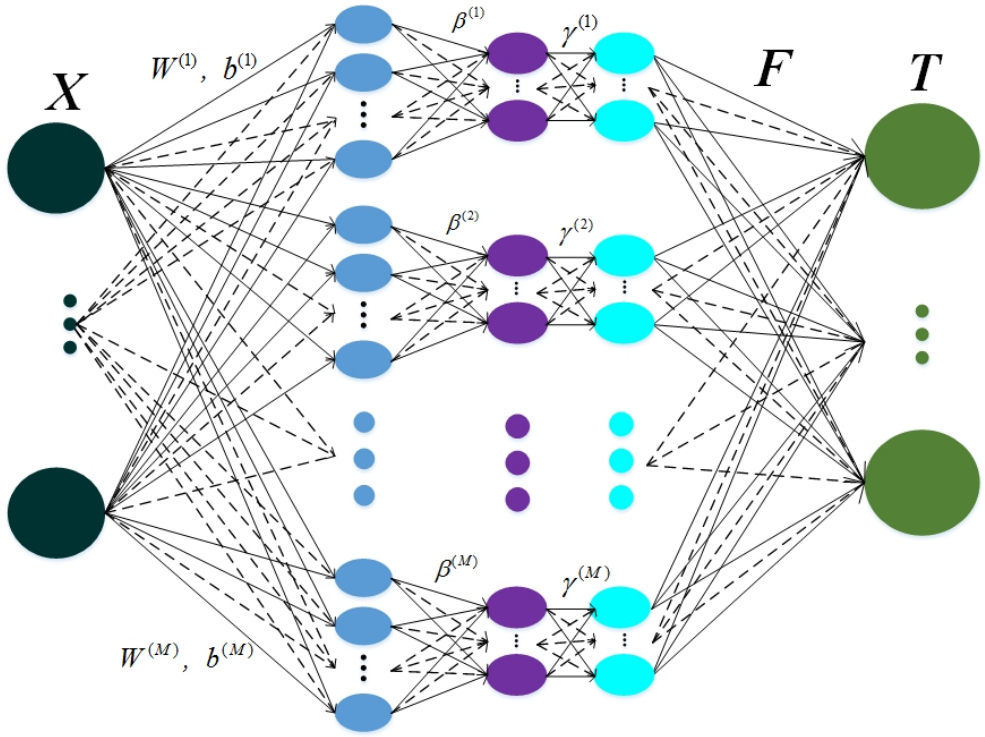

Figure 17. The proposed Extreme Learning Machine (ELM) can be seen as a three hidden layer neural network trained using the ELM algorithm.

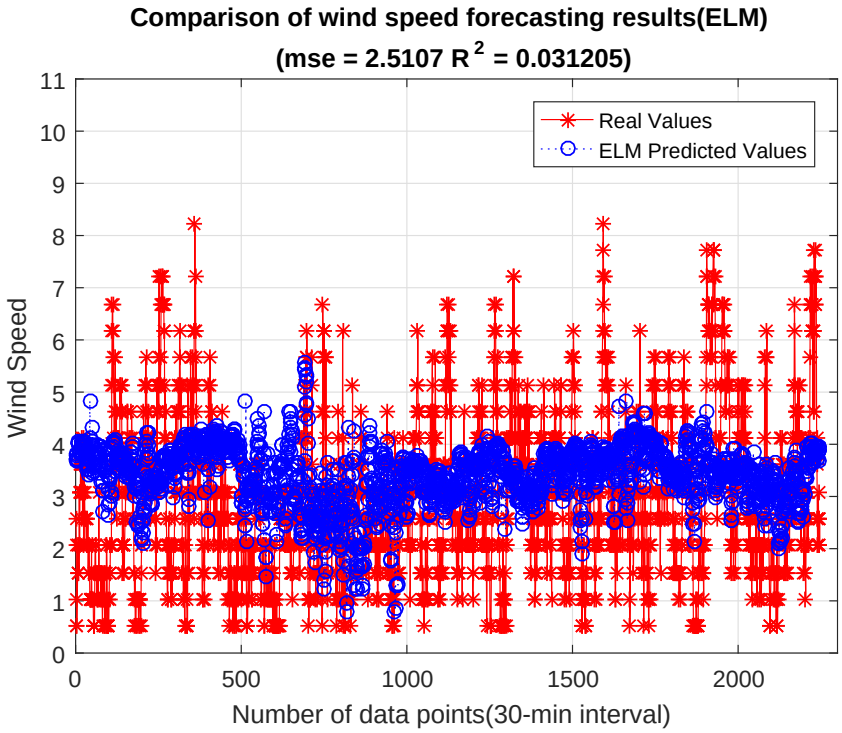

Figure 18. The portraits of comparison of wind speed forecasting results (ELM) in OSWFs in Yangshan port, Shanghai from 22 August 2017 to 22 August 2018 (number of predicted data pieces is 2248).

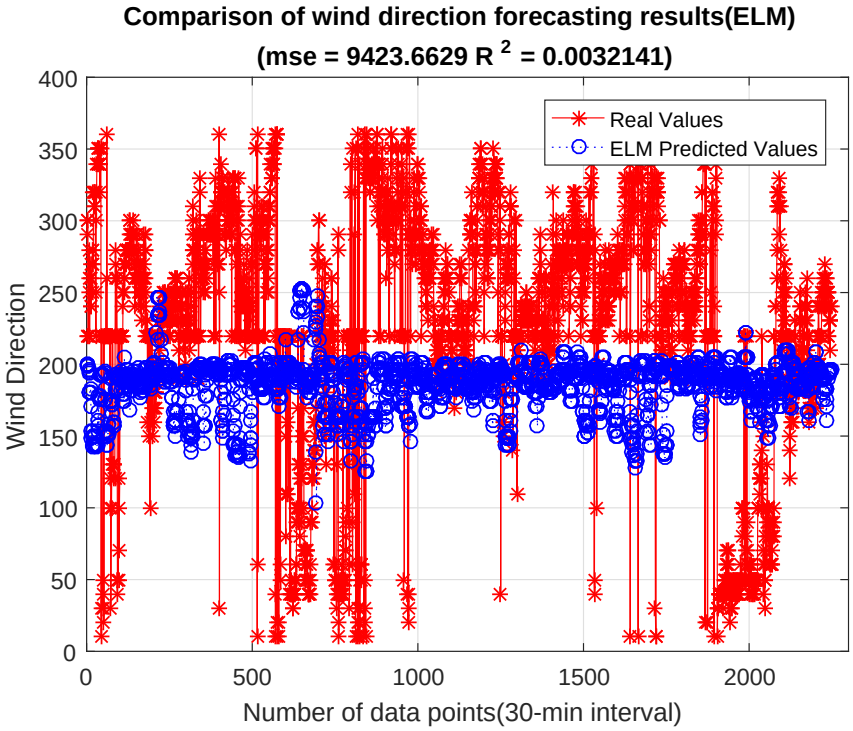

Figure 19. The portraits of comparison of wind direction forecasting results (ELM) in OSWFs in Yangshan port, Shanghai from 22 August 2017 to 22 August 2018 (number of predicted data pieces is 2248).

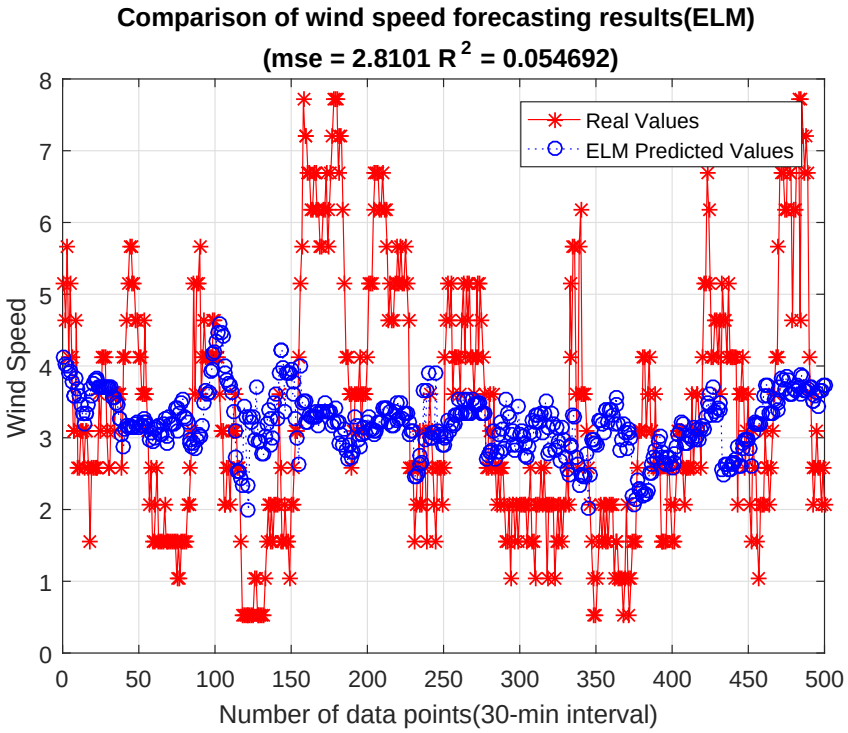

Figure 20. The portraits of comparison of wind speed forecasting results (ELM) in OSWFs in Yangshan port, Shanghai from 22 August 2017 to 22 August 2018 (number of predicted data pieces is 500).

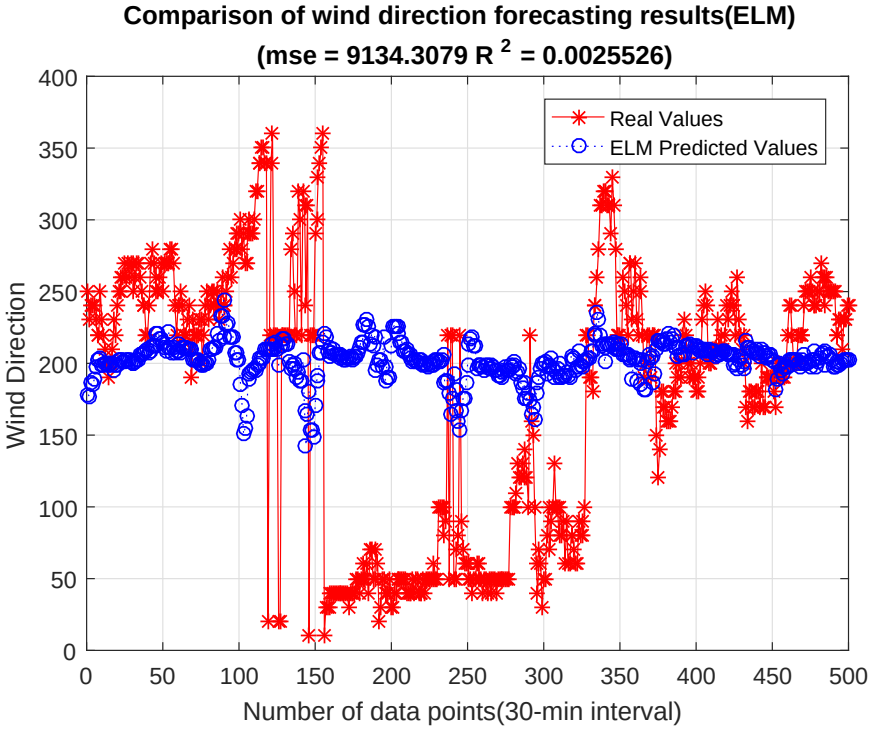

Figure 21. The portraits of comparison of wind direction forecasting results (ELM) in OSWFs in Yangshan port, Shanghai from 22 August 2017 to 22 August 2018 (number of predicted data pieces is 500).

Through the study of the Weibull Probability Distribution of Wind Velocity Data in OSWFs in Yangshan port, Shanghai, we obtain the following results. The cumulative distribution and linearized curve are plotted and shown in Figure 22, Linearized curve and fitted line comparison are shown in

Figure 23, Weibull probability density function and Cumulative Weibull probability density function are shown in Figure 24. In light of wind tower, measuring data and plotted wind speed histograms, we inferred and estimated two parameters of the Weibull distribution by maximum likelihood estimation method, i.e., $c = 3.7660$, and $k = 1.7153$. The histogram of wind speed at hub height with the fitted Weibull probability density distribution are plotted and shown in Figure 25. Wind speed at hub height conforms to the Weibull distribution.

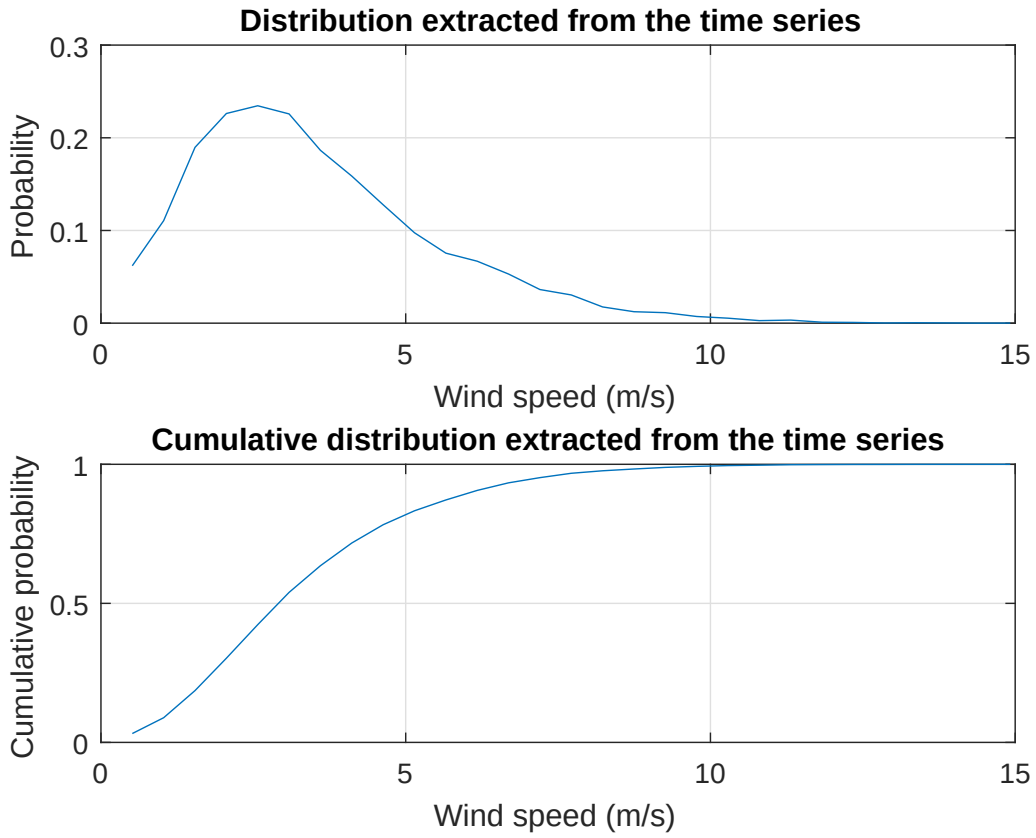

Figure 22. The portraits of distribution and cumulative distribution extracted from the time series in OSWFs in Yangshan port, Shanghai from 22 August 2017 to 22 August 2018.

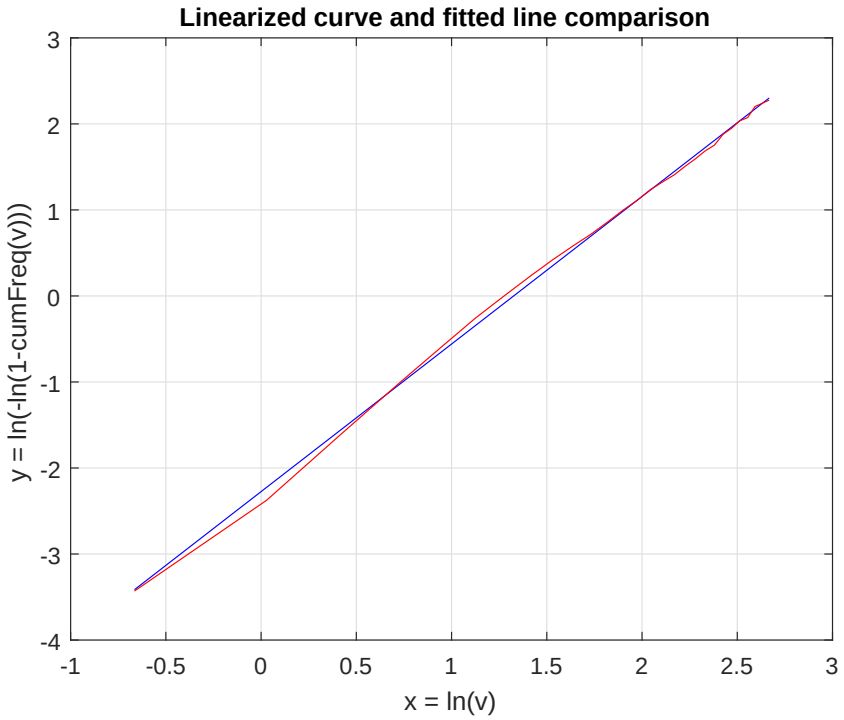

Figure 23. The portraits of linearized curve and fitted line comparison in OSWFs in Yangshan port, Shanghai from 22 August 2017 to 22 August 2018.

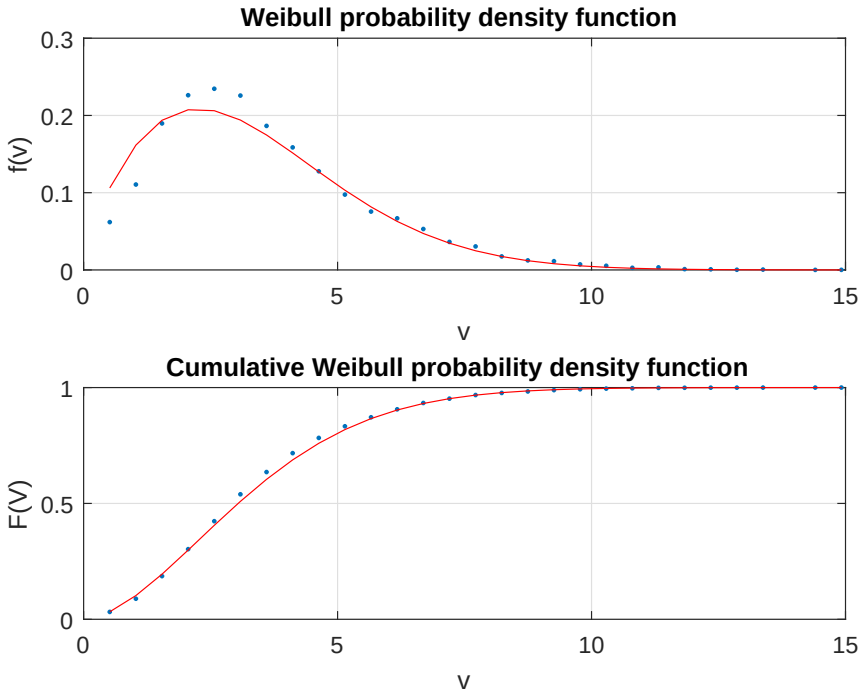

Figure 24. The portraits of Weibull and Cumulative Weibull probability density functions in OSWFs in Yangshan port, Shanghai from 22 August 2017 to 22 August 2018.

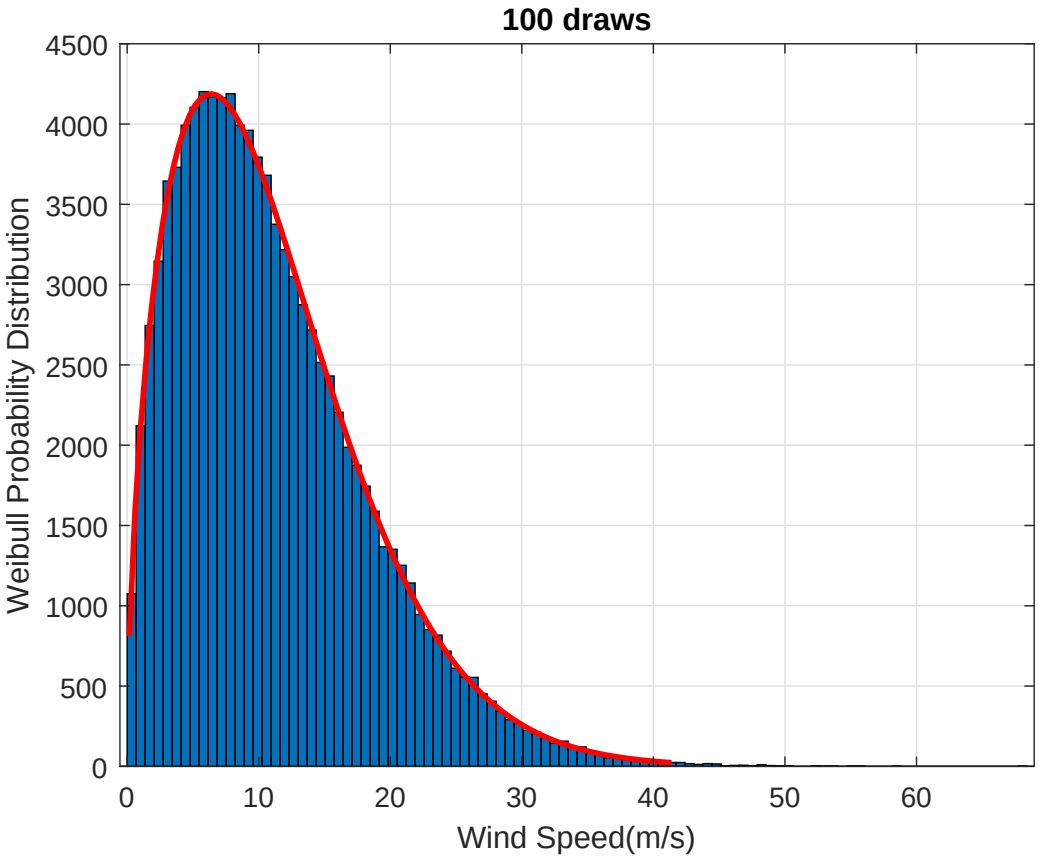

Figure 25. The portraits of wind speed histogram in hub height and the fitted Weibull probability density distribution in OSWFs in Yangshan port, Shanghai from 22 August 2017 to 22 August 2018.

7. Conclusions

From this study, we found that the feature of FGWM is simple and intuitive, while the feature of FGNDWM is complex and precise. The accuracy of the FGNDWM is inherently better than that of the FGWM. When describing the relationship between FGNDWM and FGWM, Equation (42) can reflect the essential characteristics of FGNDWM, whereas Equation (7) reflects the basic characteristics of FGWM. Equation (42) is more accurate than (7) in expressing the characteristics of the large off-shore wind farms. By taking x_{1i} into consideration, the accuracy of the FGNDWM and the FGWM can be improved. Their accuracy depends on the axial induction factor α_{ij}. The maximum Wind Speed Deficit (WSD) of this FGNDWM can be proved to be twice as large as that of the FGWM if α_{ij} and r_{0ij} are estimated by (43) and (44), respectively.

Currently, the experiments show that the accuracy of ELM predictions needs to be improved based on the actual situation in OSWFs in Yangshan port, Shanghai. In future research, we will work on hybrid wake models for near wakes and far wakes and improve the ELM predictions accuracy of large off-shore wind farms. The data assimilation and reduced order modelling will be provided in a future paper concerning induced large off-shore wind farms dynamics.

Author Contributions: Conceptualization, M.L. and H.X.; Methodology, L.P. and C.X.; Software, L.P. and C.X.; Validation, M.L., H.X. and L.P.; Formal Analysis, M.L. and H.X.; Investigation, M.L. L.P. and C.X.; Resources, M.L. and H.X.; Data Curation, M.L. and H.X.; Writing–Original Draft Preparation, L.P. and C.X.; Writing–Review and Editing, M.L. and H.X.; Visualization, L.P. and C.X.; Supervision, H.X. and L.P.; Project Administration, H.X.; Funding Acquisition, H.X..

Funding: This research was funded by the PhD research startup foundation of Wuhan University of Technology grant number 40120291, the Fundamental Research Funds for the Central Universities grant number 173118001, the Open Project Program of National Engineering Research Center for Water Transport Safety grant number A2019006, and the Open Project Program of State Key Laboratory of Ocean Engineering grant number 1812. The APC was funded by National Key Technology Research and Development Program of the Ministry of Science and Technology of China grant number 2015BAF06B01-2.

Conflicts of Interest: The authors declare no conflict of interest.

Abbreviations

The following abbreviations are used in this manuscript:

OSWFs	Off-Shore Wind Farms
WT	Wind Turbine
ELM	Extreme Learning Machine
WP	Wind Power
LES	Large-Eddy Simulation
EEA	Extended Exergy Accounting
WP	Wind Power
HAWTs	Horizontal Axis Wind Turbines
WF	Wind Farm
WE	Wind Energy
DFIG	Doubly-fed Induction Generator
PMSG	Permanent Magnet Synchronous Generator
FSIG	Fixed-Speed Induction Generator
WTPGS	Wind Turbine Power Generation System
FGWM	Frandsen Generalized Wake Model
FGNDWM	Frandsen Generalized Normal Distribution Wake Model
WSD	Wind Speed Deficit
WD	Wind Direction
AWD	Average Wind Direction

References

1. Marden, J.R.; Ruben, S.D.; Pao, L.Y. A Model-Free Approach to Wind Farm Control Using Game Theoretic Methods. *IEEE Trans. Control Syst. Technol.* **2013**, *21*, 1207–1214. [CrossRef]
2. Pao, L.Y.; Johnson, K. A tutorial on the dynamics and control of wind turbines and wind farms. In Proceedings of the American Control Conference, St. Louis, MO, USA, 10–12 June 2009; pp. 2076–2089.
3. Bitar, E.; Seiler, P. Coordinated control of a wind turbine array for power maximization. In Proceedings of the American Control Conference (ACC), Washington, DC, USA, 17–19 June 2013; pp. 2898–2904.
4. Remmers, T.; Cawkwell, F.; Desmond, C.; Murphy, J.; Politi, E. The Potential of Advanced Scatterometer (ASCAT) 12.5 km Coastal Observations for Offshore Wind Farm Site Selection in Irish Waters. *Energies* **2019**, *12*, 206. doi:10.3390/en12020206. [CrossRef]
5. Hübler, C.; Weijtjens, W.; Gebhardt, C.G.; Rolfes, R.; Devriendt, C. Validation of Improved Sampling Concepts for Offshore Wind Turbine Fatigue Design. *Energies* **2019**, *12*, 603. doi:10.3390/en12040603. [CrossRef]
6. Li, H.; Wang, J.; Lu, H.; Guo, Z. Research and application of a combined model based on variable weight for short term wind speed forecasting. *Renew. Energy* **2018**, *116*, 669–684. [CrossRef]
7. Romanic, D.; Parvu, D.; Refan, M.; Hangan, H. Wind and tornado climatologies and wind resource modelling for a modern development situated in Tornado Alley. *Renew. Energy* **2018**, *115*, 97–112. [CrossRef]
8. Ahmed, A.S. Wind energy characteristics and wind park installation in Shark El-Ouinat, Egypt. *Renew. Sustain. Energy Rev.* **2018**, *82*, 734–742. [CrossRef]
9. Aghbashlo, M.; Tabatabaei, M.; Hosseini, S.S.; Dashti, B.B.; Soufiyan, M.M. Performance assessment of a wind power plant using standard exergy and extended exergy accounting (EEA) approaches. *J. Clean. Prod.* **2018**, *171*, 127–136. [CrossRef]

10. Ahmad, T.; Basit, A.; Anwar, J.; Coupiac, O.; Kazemtabrizi, B.; Matthews, P.C. Fast Processing Intelligent Wind Farm Controller for Production Maximisation. *Energies* **2019**, *12*, 544. doi:10.3390/en12030544. [CrossRef]
11. Shakoor, R.; Hassan, M.Y.; Raheem, A.; Wu, Y.K. Wake effect modeling: A review of wind farm layout optimization using Jensen's model. *Renew. Sustain. Energy Rev.* **2016**, *58*, 1048–1059. [CrossRef]
12. Kuenzel, S.; Kunjumuhammed, L.; Pal, B.; Erlich, I. Impact of Wakes on Wind Farm Inertial Response. *IEEE Trans. Sustain. Energy* **2014**, *5*, 237–245. [CrossRef]
13. Pan, L.; Voos, H.; Li, Y.; Darouach, M.; Xu, Y.; Hu, S. A wake interaction model for the coordinated control of Wind Farms. In Proceedings of the 2015 IEEE 20th Conference on Emerging Technologies Factory Automation (ETFA), Luxembourg, 8–11 September 2015; pp. 1–7.
14. Pan, L.; Voos, H.; Pan, Y.; Darouach, M. A generalized interaction Wake Model with its variation for control in Wind Farms. In Proceedings of the 2016 35th Chinese Control Conference (CCC), Chengdu, China, 27–29 July 2016; pp. 8759–8764.
15. Pan, L.; Voos, H.; Li, Y.; Xu, Y.; Darouach, M.; Li, Z. A class of Improved Wake Interaction Model for the coordinated control of wind farms. In Proceedings of the Chinese Automation Congress (CAC), Wuhan, China, 27–29 November 2015; pp. 1322–1327.
16. He, P.; Arefifar, S.A.; Li, C.; Wen, F.; Ji, Y.; Tao, Y. Enhancing Oscillation Damping in an Interconnected Power System with Integrated Wind Farms Using Unified Power Flow Controller. *Energies* **2019**, *12*, 322. doi:10.3390/en12020322. [CrossRef]
17. March, V. Key issues to define a method of lightning risk assessment for wind farms. *Electr. Power Syst. Res.* **2017**, in press. [CrossRef]
18. Chen, K.; Song, M.; Zhang, X. The investigation of tower height matching optimization for wind turbine positioning in the wind farm. *J. Wind Eng. Ind. Aerodyn.* **2013**, *114*, 83–95. [CrossRef]
19. Sørensen, K.L.; Galeazzi, R.; Odgaard, P.F.; Niemann, H.; Poulsen, N.K. Adaptive Passivity Based Individual Pitch Control for Wind Turbines in the Full Load Region. In Proceedings of the 2014 American Control Conference, Portland, OR, USA, 4–6 June 2014; pp. 554–559.
20. Barreiro-Gomez, J.; Ocampo-Martinez, C.; Bianchi, F.; Quijano, N. Model-free control for wind farms using a gradient estimation-based algorithm. In Proceedings of the 2015 European Control Conference (ECC), Linz, Austria, 15–17 July 2015; pp. 1516–1521.
21. Long, M.; Becerra, M.; Thottappillil, R. On the attachment of dart lightning leaders to wind turbines. *Electr. Power Syst. Res.* **2017**, *151*, 432–439. [CrossRef]
22. Thukaram, D. Accurate modeling of doubly fed induction generator based wind farms in load flow analysis. *Electr. Power Syst. Res.* **2018**, *155*, 363–371.
23. Farajzadeh, S.; Ramezani, M.H.; Nielsen, P.; Nadimi, E.S. Statistical modeling of the power grid from a wind farm standpoint. *Electr. Power Syst. Res.* **2017**, *144*, 150–156. [CrossRef]
24. Tian, L.; Zhu, W.; Shen, W.; Zhao, N.; Shen, Z. Development and validation of a new two-dimensional wake model for wind turbine wakes. *J. Wind Eng. Ind. Aerodyn.* **2015**, *137*, 90–99. [CrossRef]
25. Park, J.; Law, K.H. A data-driven, cooperative wind farm control to maximize the total power production. *Appl. Energy* **2016**, *165*, 151–165. [CrossRef]
26. Marseglia, G.R.; Arbasini, A.; Grassi, S.; Raubal, M.; Raimondo, D.M. Optimal placement of wind turbines on a continuous domain: An MILP-based approach. In Proceedings of the American Control Conference (ACC), Chicago, IL, USA, 1–3 July 2015; pp. 5010–5015.
27. van Dam, F.; Gebraad, P.; van Wingerden, J.W. A maximum power point tracking approach for wind farm control. In Proceedings of the Science of Making Torque from Wind, Oldenburg, Germany, 9–11 October 2012.
28. Chen, J. Development of offshore wind power in China. *Renew. Sustain. Energy Rev.* **2011**, *15*, 5013–5020. doi:10.1016/j.rser.2011.07.053. [CrossRef]
29. Zhixin, W.; Chuanwen, J.; Qian, A.; Chengmin, W. The key technology of offshore wind farm and its new development in China. *Renew. Sustain. Energy Rev.* **2009**, *13*, 216–222. doi:10.1016/j.rser.2007.07.004. [CrossRef]
30. Ebrahimi, F.; Khayatiyan, A.; Farjah, E. A novel optimizing power control strategy for centralized wind farm control system. *Renew. Energy* **2016**, *86*, 399–408. [CrossRef]
31. Song, Z.; Zhang, Z.; Chen, X. The decision model of 3-dimensional wind farm layout design. *Renew. Energy* **2016**, *85*, 248–258. [CrossRef]

32. Varzaneh, S.G.; Abedi, M.; Gharehpetian, G. A new simplified model for assessment of power variation of DFIG-based wind farm participating in frequency control system. *Electr. Power Syst. Res.* **2017**, *148*, 220–229. [CrossRef]
33. Hossain, M.E. A non-linear controller based new bridge type fault current limiter for transient stability enhancement of DFIG based Wind Farm. *Electr. Power Syst. Res.* **2017**, *152*, 466–484. [CrossRef]
34. Yao, J.; Li, J.; Guo, L.; Liu, R.; Xu, D. Coordinated control of a hybrid wind farm with PMSG and FSIG during asymmetrical grid fault. *Int. J. Electr. Power Energy Syst.* **2018**, *95*, 287–300. [CrossRef]
35. Li, D.Y.; Li, P.; Cai, W.C.; Song, Y.D.; Chen, H.J. Adaptive Fault Tolerant Control of Wind Turbines with Guaranteed Transient Performance Considering Active Power Control of Wind Farms. *IEEE Trans. Ind. Electron.* **2017**, *65*, 3275–3285. [CrossRef]
36. Chaurasiya, P.K.; Ahmed, S.; Warudkar, V. Comparative analysis of Weibull parameters for wind data measured from met-mast and remote sensing techniques. *Renew. Energy* **2018**, *115*, 1153–1165. [CrossRef]
37. Atighechi, H.; Hu, P.; Ebrahimi, S.; Lu, J.; Wang, G.; Wang, L. An effective load shedding remedial action scheme considering wind farms generation. *Int. J. Electr. Power Energy Syst.* **2018**, *95*, 353–363. [CrossRef]
38. Suganthi, S.; Devaraj, D.; Ramar, K.; Thilagar, S.H. An Improved Differential Evolution algorithm for congestion management in the presence of wind turbine generators. *Renew. Sustain. Energy Rev.* **2018**, *81*, 635–642. [CrossRef]
39. Wan, C.; Xu, Z.; Pinson, P.; Dong, Z.Y.; Wong, K.P. Probabilistic forecasting of wind power generation using extreme learning machine. *IEEE Trans. Power Syst.* **2014**, *29*, 1033–1044. [CrossRef]
40. Nikolić, V.; Motamedi, S.; Shamshirband, S.; Petković, D.; Ch, S.; Arif, M. Extreme learning machine approach for sensorless wind speed estimation. *Mechatronics* **2016**, *34*, 78–83. [CrossRef]
41. Lazarevska, E. Wind speed prediction with extreme learning machine. In Proceedings of the 2016 IEEE 8th International Conference on Intelligent Systems (IS), Sofia, Bulgaria, 4–6 September 2016; pp. 154–159.
42. Wu, S.; Wang, Y.; Cheng, S. Extreme learning machine based wind speed estimation and sensorless control for wind turbine power generation system. *Neurocomputing* **2013**, *102*, 163–175. [CrossRef]
43. Frandsen, S.; Barthelmie, R.; Pryor, S.; Rathmann, O.; Larsen, S.; Højstrup, J.; Thøgersen, M. Analytical modelling of wind speed deficit in large offshore wind farms. *Wind Energy* **2006**, *9*, 39–53. [CrossRef]
44. Pookpunt, S.; Ongsakul, W. Optimal placement of wind turbines within wind farm using binary particle swarm optimization with time-varying acceleration coefficients. *Renew. Energy* **2013**, *55*, 266–276. [CrossRef]
45. Iowa State University of Science and Technology The Iowa Environmental Mesonet (IEM). Available online: http://mesonet.agron.iastate.edu/ (accessed on 5 March 2019).
46. Huang, G.B.; Zhu, Q.Y.; Siew, C.K. Extreme learning machine: A new learning scheme of feedforward neural networks. *Neural Netw.* **2006**, *2*, 985–990.